

2008

Convective systems in the 2006 West African monsoon: a radar study

B. Nicholas Guy
San Jose State University

Follow this and additional works at: https://scholarworks.sjsu.edu/etd_theses

Recommended Citation

Guy, B. Nicholas, "Convective systems in the 2006 West African monsoon: a radar study" (2008). *Master's Theses*. 3509.
DOI: <https://doi.org/10.31979/etd.uhwq-st4v>
https://scholarworks.sjsu.edu/etd_theses/3509

This Thesis is brought to you for free and open access by the Master's Theses and Graduate Research at SJSU ScholarWorks. It has been accepted for inclusion in Master's Theses by an authorized administrator of SJSU ScholarWorks. For more information, please contact scholarworks@sjsu.edu.

CONVECTIVE SYSTEMS IN THE 2006 WEST AFRICAN MONSOON:
A RADAR STUDY

A Thesis

Presented to

The Faculty of the Department of Meteorology

San Jose State University

In Partial Fulfillment

of the Requirements for the Degree

Master of Science

by

B. Nicholas Guy

August 2008

UMI Number: 1459698

INFORMATION TO USERS

The quality of this reproduction is dependent upon the quality of the copy submitted. Broken or indistinct print, colored or poor quality illustrations and photographs, print bleed-through, substandard margins, and improper alignment can adversely affect reproduction.

In the unlikely event that the author did not send a complete manuscript and there are missing pages, these will be noted. Also, if unauthorized copyright material had to be removed, a note will indicate the deletion.

UMI[®]

UMI Microform 1459698

Copyright 2008 by ProQuest LLC.

All rights reserved. This microform edition is protected against unauthorized copying under Title 17, United States Code.

ProQuest LLC
789 E. Eisenhower Parkway
PO Box 1346
Ann Arbor, MI 48106-1346

© 2008

B. Nicholas Guy

ALL RIGHTS RESERVED

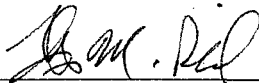
APPROVED FOR THE DEPARTMENT OF METEOROLOGY



Dr. Craig B. Clements

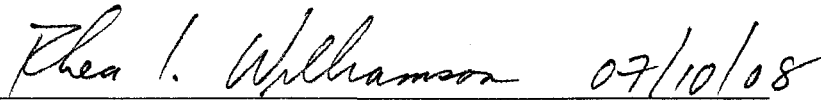


Dr. Eugene C. Cordero



Dr. Thomas M. Rickenbach, East Carolina University

APPROVED FOR THE UNIVERSITY



ABSTRACT

CONVECTIVE SYSTEMS IN THE 2006 WEST AFRICAN MONSOON: A RADAR STUDY

by B. Nicholas Guy

The 2006 African Monsoon Multidisciplinary Activities Intensive Observational Period provided a wealth of information regarding the onset and development of the monsoon season over the Sahel region of West Africa. Enhanced understanding of predictability and variability of monsoon is scientifically and socioeconomically beneficial. Radar observations near Niamey, Niger documented the structure, motion, and precipitation of convective cloud systems during the monsoon season, with particular focus on mesoscale convective systems.

A thorough review and analysis of non-meteorological echo removal by the quality control algorithm, shown to be largely successful, is a main focus of this thesis. Resulting corrected reflectivity data were used to construct rainrate timeseries to examine the progression of convective activity throughout the West African monsoon season. It was found that mesoscale convective systems contributed the majority of rainfall and cloud cover during the season and exhibited variability linked to the diurnal heating cycle and African easterly waves.

ACKNOWLEDGEMENTS

I would like to acknowledge the members of my thesis committee: Drs. Tom Rickenbach, Craig Clements, and Eugene Cordero. Their careful review and suggestions for this thesis were invaluable. I would also like to thank the Committee for their very personable demeanors, combining both humor and candor in meetings and written correspondence.

I would like to specifically thank Dr. Tom Rickenbach for the opportunity to work on this project and for his unwavering guidance and advice, even across great distances. His selflessness with time, reliability, and dedicated mentorship is sincerely appreciated.

This thesis also benefited from personal communication with David Wolff, Bart Kelley, and Jason Pippitt (in order of contact) from Goddard Space Flight Center. Their valuable input with regards to the installation and use of the quality control software employed was essential to the outcome of this thesis.

Next, I would like to thank the members of the San Jose State University faculty and students for making this program such a positive experience. I have enjoyed the last two years immensely, establishing friends and colleagues of the highest caliber.

Finally, and most gratefully, I would like to extend my deepest thanks to my wife, Carrie, and daughter, Micah, for always being there to make me laugh and smile. Their endless support and encouragement made this possible; and their willingness to move for the next step in education reminds me how fortunate I am to have them in my life.

TABLE OF CONTENTS

LIST OF TABLES	vii
LIST OF FIGURES.....	viii
1. Introduction.....	1
2. Background.....	5
a. Tropical convection	5
b. WAM and rainfall.....	9
c. African easterly waves.....	13
d. Radar data quality control.....	14
3. Methodology	18
a. Data	18
b. Processing raw data	19
c. Data classification (qualitative).....	24
d. Data quality control (quantitative)	30
e. Rainfall estimation and convective-stratiform partitioning	39
4. Results	42
a. QC performance	42
b. Rainfall estimates	54
c. Rainfall and area coverage	62
d. Diurnal composites	64
e. Vertical structure	72
f. SLMCSs and AEWs.....	80
5. Conclusion	81
REFERENCES	84
APPENDICES	91
Appendix A List of Symbols	91
Appendix B List of Acronyms	92

LIST OF TABLES

Table 1. MIT C-band radar characteristics.....	3
Table 2. Software packages utilized to process MIT radar data for the 2006 AMMA project.....	18
Table 3. Software packages utilized.....	22
Table 4. Monthly distribution of and total MCS-scale events for the 2006 West African monsoon season.	26
Table 5. MCS event times for the 2006 West African monsoon season. Niamey, Niger local time is UTC + 1hr.....	28
Table 6. GVS Level 1 quality control software (1C51) parameters resolved for quality control algorithm of the 2006 AMMA radar dataset.	33
Table 7. Mean monthly rainfall and total area per month and seasonally bias calculations during the 2006 West African monsoon season.	49

LIST OF FIGURES

Fig. 1	AMMA implementation region in the Sahel region of West Africa. Location of MIT radar is indicated by red X , with the scan region represented by the red circle.....	2
Fig. 2	Photograph of MIT radar site at Niamey, Niger airport. Location shown in Fig. 1. Photograph by Tom Rickenbach.....	2
Fig. 3	Schematic of the mature phase of a tropical mesoscale convective system. Cloud extent is indicated by light gray shading. Solid black region is convective precipitation, while the vertical lines in the medium shade indicate stratiform precipitation. Small, straight arrows represent updrafts and downdrafts, while large open arrows show ascent and subsidence of stratiform region on the Mesoscale. Wavy lines are representative of long- and short-wave radiation, LW and SW, respectively (adapted from Houze 2004).	6
Fig. 4	Vertical cross section of a squall line mesoscale convective system conceptual model, oriented perpendicular to the convective line. H and L show centers of positive and negative pressure perturbations, respectively. Shading indicates intermediate (medium) and strong (dark) radar reflectivity regions. Arrows indicate general flow patterns (adapted from Houze 2004).	7
Fig. 5	Schematic of a fully developed West African monsoon, displayed as a latitudinal cross section. The ascending Saharan air layer is shown to flow toward the low created by surface heating located at the ITCZ. Monsoonal flow is shown to be northward and the African Easterly jet forms aloft at the leading edge of the ITCZ (adapted from Hall and Peyrille 2006).	11
Fig. 6	Diagram of radar beam propagation in various refractivity gradient regimes. It can be seen that superrefraction and ducting occur in the lowest elevation scan angles (modified from Pratte <i>et al.</i> 1996).	15
Fig. 7	Illustration of sampling volume used for Cartesian transformation of radar data from polar scan coordinates. Solid dots are projection points, while the open dot represents a Cartesian grid location on consecutive elevation scan planes, k and k + 1. The angle along azimuth is θ , while Φ is the elevation angle (modified from Mohr <i>et al.</i> 1986).....	21
Fig. 8	Flowchart depicting the order of software operation according to the decision tree structure indicated.	23
Fig. 9	Constant altitude plan position indicator radar reflectivity maps at 1 km height, containing a) a MCS scale system and b) a sub-MCS scale system, occurring on	

	14 July and 6 July 2006, respectively. Radar range rings are given every 50 km.	25
Fig. 10	Observed squall line mesoscale convective system on 22 August 2006, representative of many MCS scale systems observed over the course of this study. This particular system exhibited a classic bow structure of the leading convective cores, with massive trailing stratiform precipitation. Radar range rings are given every 50 km.	27
Fig. 11	A unique stratiform precipitation event that occurred 9 September 2006. There was no preceding or subsequent convective system to account for widespread stratiform observed. Radar range rings are given every 50 km.....	29
Fig. 12	Radar echo maps showing a sample of a) no quality control filter, b) region-specific default parameters provided by GSFC, and c) region-specific special case parameters applied for spurious radar echo removal resolved by SJSU.	36
Fig. 13	Radar reflectivity data displayed as a) raw data and b) quality controlled data. Spurious echo was removed via quality control efforts employing GVS 1C51 software. Radar range rings are given every 50 km.	38
Fig. 14	A large squall line mesoscale convective system event plotted as a) reflectivity and b) convective-stratiform component map. The reflectivity map is generated from corrected radar data, while the convective-stratiform map is resultant from a partitioning algorithm operating on corrected radar data. A linear, strong leading convective edge is apparent with a large trailing stratiform component. The color gradation in a) is related to reflectivity value (dBZ), while in b) red and yellow represent areas of convection and blue show areas of stratiform. ...	41
Fig. 15	Examples of before (a-c) and after (d-f) quality control of radar reflectivity scans containing a) weak noise, b) strong noise, and c) noise caused by morning inversions by the GVS 1C51 algorithm. Radar range rings are given every 50 km.	43
Fig. 16	Examples of before (a-c) and after (d-f) quality control of radar reflectivity scans containing 2nd trip echo a) in pure noise, b) preceding MCS approach, and c) embedded in a precipitation signal by the GVS 1C51 algorithm. Radar range rings are given every 50 km.	44
Fig. 17	Examples of before (a-b) and after (c-d) quality control of radar reflectivity scans containing a) isolated and b) scattered convection by the GVS 1C51 algorithm. Radar range rings are given every 50 km.....	45

Fig. 18	Examples of before (a-b) and after (c-d) quality control of radar reflectivity scans containing a SLMCS precipitation signal as the system a) enters the scan range and b) passes over the center of the radar scan area by the GVS 1C51 algorithm. Radar range rings are given every 50 km.....	46
Fig. 19	Examples of before (a-b) and after (c- d) quality control of radar reflectivity scans containing stratiform precipitation signal a) not associated with a large-scale system and b) trailing a SLMCS by the GVS 1C51 algorithm. Radar range rings are given every 50 km.....	47
Fig. 20	Flowchart of the decision tree for quality control algorithm application and parameter set used for various radar scan situations.....	48
Fig. 21	Relative frequency of rainfall bias (in percent) for July a) MCS and d) sub-MCS scale events; August b) MCS and e) sub-MCS scale events; and September c) MCS and f) sub-MCS scale events.....	51
Fig. 22	Relative frequency of total echo cover bias (in percent) for July a) MCS and d) sub-MCS scale events; August b) MCS and e) sub-MCS scale events; and September c) MCS and f) sub-MCS scale events.....	53
Fig. 23	July radar reflectivity-estimated rainfall rate for total (black), convective (red) and stratiform (blue) precipitation components. This 10 minute interval data indicates the temporal passage of rain events, most with close connection to MCSs.....	55
Fig. 24	August radar reflectivity-estimated rainfall rate for total (black), convective (red) and stratiform (blue) precipitation components. This 10 minute interval data indicates the temporal passage of rain events, most with close connection to mesoscale MCSs.....	56
Fig. 25	September radar reflectivity-estimated rainfall rate for total (black), convective (red) and stratiform (blue) precipitation components. This 10 minute interval data indicates the temporal passage of rain events, most with close connection to MCSs.....	57
Fig. 26	Duration of MCSs throughout the West African monsoon season. Regions are divided (heavy vertical dashed line) based on month in which system occurred.	59
Fig. 27	Spectral analyses of monthly rainfall time series data to assess periodicity of dataset. Fourier transform algorithm analysis of rainfall frequency is shown for a) July, b) August, and c) September.....	61

Fig. 28	Monthly convective (dark) and stratiform (light) rainfall portions of total precipitation in MCSs, in terms of radar reflectivity-converted rainrate per hour.	62
Fig. 29	Monthly convective (dark) and stratiform (light) portions of total areal coverage encompassed by MCSs. Each month is normalized separately against total area covered by MCSs.....	64
Fig. 30	Seasonal diurnal composite of average rainfall for SLMCSs. Seasonal total (black) of July (red), August (blue), and September (green) are plotted as a function of hour of day.....	65
Fig. 31	Seasonal diurnal composite of average rainfall for sub-MCS events. Seasonal total (black) of July (red), August (blue), and September (green) are plotted as a function of hour of day.....	66
Fig. 32	Frequency histogram of SLMCS passage over radar during the West African monsoon season in Niamey, Niger.	68
Fig. 33	Isolated local convection in south and western portion of the radar scan domain during the afternoon of 10 July 2006. Radar range rings are given every 50 km.	70
Fig. 34	Rainfall estimates for a) January (winter), b) April (spring), c) August (summer), and d) November (fall) derived from satellite and rain gauge data. Plots generated by the Climate Prediction Center (http://www.cpc.ncep.noaa.gov/products/fews/rfe.shtml).	71
Fig. 35	MIT radar mean vertical reflectivity profile for the 2006 West African monsoon season (black); and sub-divided by month: July (green) and August (red) and September (blue). The top panel represents all events, while the middle and bottom panels show convective and stratiform components of the events, respectively.....	74
Fig. 36	MIT radar mean vertical reflectivity profile for the 2006 West African monsoon season (solid line); and sub-divided into SLMCS (dotted line) and sub-MCS (dashed line) scale components. The top panel represents all events, while the middle and bottom panels show convective and stratiform components of the events, respectively.....	77
Fig. 37	MIT radar mean 30 dBZ contour height time series (solid line) for a) July, b) August, and c) September 2006. The dashed line indicates daily rainfall normalized against the monthly maximum.	79

1. Introduction

The African Monsoon Multidisciplinary Activities (AMMA) is an international project focused on the expansion of many facets of knowledge regarding the West African Monsoon (WAM), including interaction of the WAM with the physical, chemical, and biological environment. Scientific insight into the variability and predictability of the WAM, onset mechanisms, and hydrological budget is essential. Drought conditions, as seen in the 1970s in the Sahel region, can have devastating consequences to West African society by advancing desertification which affects agriculture and domestic needs. The AMMA project represents an effort that continues scientific research established in the Global Atmospheric Research Project (GARP) Atlantic Tropical Experiment (GATE; Kuettner 1974) and West African Monsoon Experiment (WAMEX; Dhonneur 1978) in the 1970s that provided a large volume of data regarding atmospheric structure and features over Africa. In the 1990s, the Etudes des Precipitations par Satellite (EPSAT) project provided a surface rainfall dataset (Lebel *et al.* 1992) which allowed further study of continental Africa, with focus on the Sahel region using a raingauge network (EPSAT-Niger).

The AMMA Intensive Observational Period, which took place during the summer of 2006, provided a wealth of information regarding the onset and development of the monsoon season over the Sahel region of West Africa (Redelsperger *et al.*, 2006). Radar observations near Niamey, Niger (Figs. 1-2) during AMMA documented the structure, motion, and precipitation of convective cloud systems during the monsoon

season. A radar-based analysis of convective storm development and propagation, with particular focus on mesoscale convective systems (MCSs), was performed.

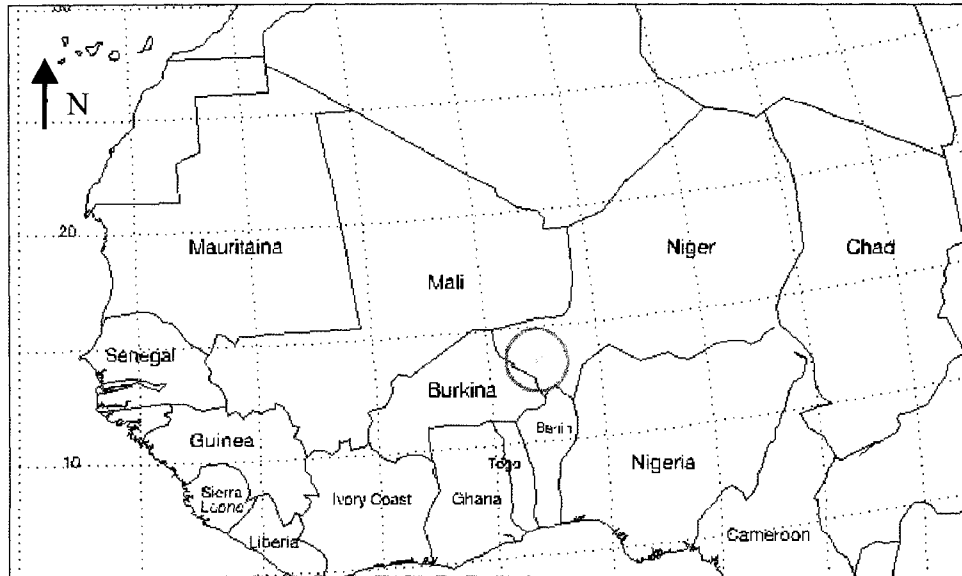


Fig. 1 AMMA implementation region in the Sahel region of West Africa. Location of MIT radar is indicated by red X , with the scan region represented by the red circle.



Fig. 2 Photograph of MIT radar site at Niamey, Niger airport. Location shown in Fig. 1. Photograph by Tom Rickenbach.

Radar data were collected with the Massachusetts Institute of Technology (MIT) C-band Doppler radar from June – September 2006. Radar characteristics can be found in Table 1. At the beginning of the experiment, radar setup and optimization was performed, where various setup configurations (e.g. Doppler measurements and scanning strategies) were tested to reveal optimum performance for a given sampling region. The dataset usable for this study (full volume scans) encompassed 5 July – 27 September 2006 and was collected on-site in Interactive Radar Information System (IRIS) format developed by the Sigmec Corporation. An important component of this thesis was the description and implementation of quality control (QC) of the radar data to allow further detailed analysis.

Table 1. MIT C-band radar characteristics.

Operating Frequency	5590 MHz
Antenna Diameter	8 ft
Antenna 3dB beamwidth	1.2 deg
Peak transmitter power	500 kW
Total power consumption	~10 kW

Previous studies have analyzed MCS rainfall and structure for the Sahel region using satellite and rain gauge observational datasets or have focused on the dynamics of individual storm systems. This study analyzes the raw radar dataset and classifies precipitation into large organized cloud systems and isolated convective cells. Though they can be related, these two unique phenomena represent different scales of convective forcing and impact on the large-scale environment. The precipitation categories must be treated separately to accurately infer monsoon season characteristics and effects. Isolated convective updrafts are too small in scale to generate significant effects on the large scale

environment; however, more extensive MCS events impact the large-scale environment due to energy and momentum transport via upward air motion required to maintain a steady state mature MCS in an unstably stratified and sheared environment (Moncrieff 1981). Initial inflow and ascent may result from gravity wave response to MCS heating (Schmidt and Cotton 1990). Observational ground-based radar data provided a better understanding of MCS and non-MCS precipitation, through qualitative and quantitative examination of the 2006 WAM season via rainfall classification and characteristics; and estimation and statistics, respectively. Radar-inferred precipitation represents a bridge between satellite and rain gauge observations, both on scale and quantitative levels. Precipitation analysis from sub-MCS and MCS-scale events allowed exploration of the connection between convection and larger scale mechanisms, such as African easterly waves (AEWs). Results of this study will provide important insight into the role of MCSs in the WAM season and guidance in defining characteristics for climatological analysis of the Sahel region.

2. Background

a. Tropical convection

Tropical cumulus convection occurs over a wide range of spatial scales, from individual, isolated convective cores (a hundred meters to a few kilometers; Houze 1993) to organized systems thousands of kilometers wide called mesoscale convective complexes (MCCs; Maddox 1980; Houze 1993). The tropics provide continual heating from the surface, which results in strong vertical mixing and can lead to substantial instability. Organization of very large systems into MCCs is less prevalent than smaller scale events. MCCs were estimated to provide only about 15% of total convective cloud cover in a study of the Sahelian region (Mathon and Laurent 2001).

A common manifestation of tropical convection occurs on the MCC scale. When individual convective cores organize into clusters with a single cloud shield, they are known as a MCS. Cotton and Anthes (1989) and Houze (1993) define a MCS as a group of organized thunderstorms with a contiguous precipitation region (Rickenbach and Rutledge 1998) of at least 100 km and can have a horizontal length of several hundreds of kilometers. Precipitation from a MCS divides into two distinct regions: convective, intense, vertically extended cores; and stratiform, formed from dissipation of convective cells or mesoscale ascent (Houze 2004). MCS organization can develop linearly, as multiple thunderstorms align along a single axis, or nonlinearly in erratically shaped clusters.

Figure 3 shows a schematic of a mature tropical MCS. The spatial disparity between convective and stratiform precipitation regions can be seen, along with the

general motions indicated by arrows. Small straight arrows indicate updrafts and downdrafts, while large open arrows show comparatively weak ascent and subsidence of the stratiform region on the mesoscale where vapor deposition and evaporation drive the precipitation process. Long- and short-wave radiation (LW and SW, respectively) are shown by wavy arrows. The extent of the cloud cover is indicated by the light gray shading.

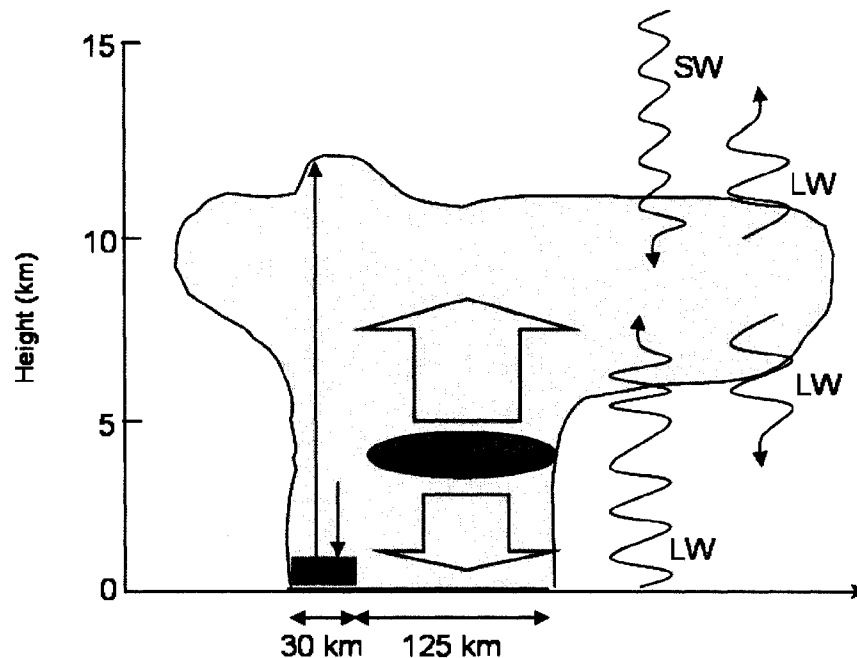


Fig. 3 Schematic of the mature phase of a tropical mesoscale convective system. Cloud extent is indicated by light gray shading. Solid black region is convective precipitation, while the vertical lines in the medium shade indicate stratiform precipitation. Small, straight arrows represent updrafts and downdrafts, while large open arrows show ascent and subsidence of stratiform region on the Mesoscale. Wavy lines are representative of long- and short-wave radiation, LW and SW, respectively (adapted from Houze 2004).

Figure 4 represents a cross sectional view of the kinematic, microphysical and radar echo representation of a linear MCS. New cells are formed in front of mature and decaying convective cores in the direction of nominal system motion. The shading

represents radar echo, with darker shading representing stronger reflectivity. General flow patterns are shown by arrows, indicating descending rear inflow and ascending front-to-rear flow.

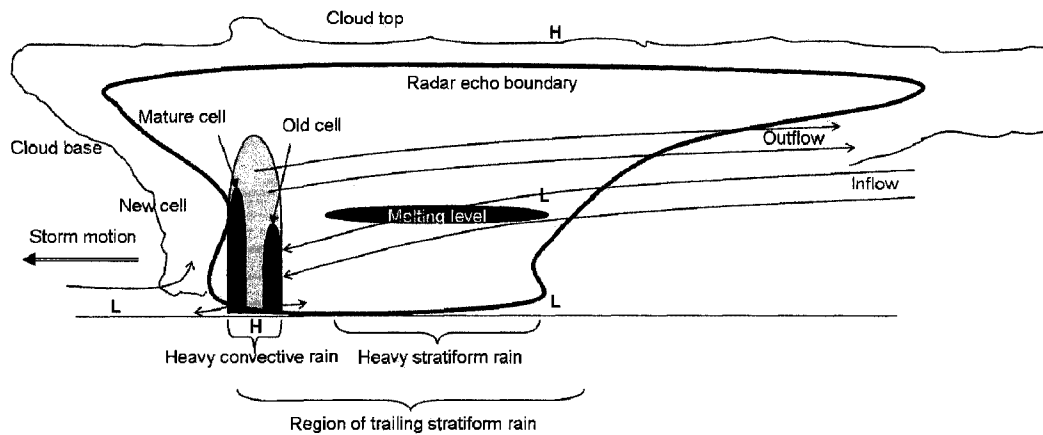


Fig. 4 Vertical cross section of a squall line mesoscale convective system conceptual model, oriented perpendicular to the convective line. H and L show centers of positive and negative pressure perturbations, respectively. Shading indicates intermediate (medium) and strong (dark) radar reflectivity regions. Arrows indicate general flow patterns (adapted from Houze 2004).

Motions that arise due to the MCS are illustrative of heat and momentum transport associated with these systems. The degree to which convective cells in MCSs are organized into lines results in vastly different heat and momentum flux aspects. Convective and stratiform components result in different heat and momentum transport (Houze 1993). The convective portion produces net heating at all levels, where cumulus scale updrafts transport heat (condensation) and low level horizontal momentum upward, but downdrafts are insufficient to remove condensational heating in the updraft. The upper levels of the stratiform region show net heating due to condensation, while levels lower in the troposphere cool from evaporation and melting processes. Rear inflow of low equivalent potential temperature air below the trailing anvil cloud descends toward

the convective line, transporting opposing momentum downward. These processes in a linear MCS cause increased momentum against line propagation at upper levels and decreased momentum with line propagation at lower levels (LeMone *et al.* 1984; Rickenbach and Rutledge 1998).

These transports have a substantial impact on the thermodynamic and dynamic structure of the free environment. MCS-created disturbances, over a range of wavelengths, have the net effect to displace environmental mass downward (Mapes and Houze 1995; Houze 2004). Shorter wavelength disturbances are able to feed new convection near a MCS, due to longer time near the system. Longer wavelength disturbances are able to escape the immediate MCS area and interact with the environment. Mid-level convergence associated with the stratiform portion of linear MCS events induced mesoscale upward motion that augmented non-convective rain (Mapes and Houze 1993). It has been shown that heating profiles of organized cloud clusters produce more realistic large scale circulations (e.g. Walker Circulation), than heating profiles of individual convective towers (Hartmann *et al.* 1984). A thorough treatment of MCSs can be found in Houze (2004).

Many studies have proposed MCS classifications using different methods and requirements, with infrared (IR) satellite and radar the two most common media used to create a classification construct. IR satellite measurements offer wide view angles, enabling continuous monitoring of MCS scale systems throughout their lifetime. A large number of studies have used cloud top brightness temperatures related to specific MCS organization and evolution. Radar measurements, while more limited in sample region

extent, allow greater internal detail of MCS structure and resolve mesoscale and sub-mesoscale features more easily, such as gust fronts and patterns of precipitation organization. Analyses during the formative and development stage and during the mature stage provide different classifications of linear MCSs (Bluestein and Jain 1985; Parker and Johnson 2000). As detailed in Rickenbach and Rutledge (1998), classifications vary widely, dependent upon the goals and location of study.

There are widely used categorical classifications, however, such as squall line MCSs (SLMCSs), described in Hamilton and Archbold (1945) and based on observational radar data acquired during field experiments (Zisper 1977; Houze 1977). Even these SLMCSs offer a wide variety of classification standards [see Table 1 in Rowell and Milford (1993)]. Mathon *et al.* (2002) described a new classification called the organized convective system (OCS), which was defined via satellite observations, but based on widely accepted radar-based characteristics. This ensured that the majority of squall line system occurrences were grouped in a single definition, as previous classifications may divide the dataset. This disparity of definition criteria results in a subjective classification system, largely dependent upon scope and regional area of study. The classification system used in this study will be further discussed in section 3c.

b. WAM and rainfall

West Africa is characterized by zonally-oriented climate zones, with no large topographical features to impinge atmospheric flow. The migration of the monsoon into these banded zones results in relatively zonally-homogenous monsoon features (Hall and

Peyrille 2006). A thermally induced low pressure trough inherent over the African continent shifts as a function of seasonality (i.e. a large scale dynamic response to variable heating patterns). The intertropical convergence zone (ITCZ), where the surface pressure trough and confluence zone are located, acts as a barrier separating the dry northern desert region from the moist southern tropical region. During boreal winter, the ITCZ is positioned near the equator and allows the dry, northeasterly winds originating in the desert (Harmattan winds) to propagate further south confining precipitation to the lower portion of the continent. Northward movement of the ITCZ occurs during boreal summer, which advects moisture northward (Hastenrath 1991) to the normally dry sub-Saharan Sahel region.

A schematic of the fully developed WAM is shown in Fig. 5, where it can be seen that the ITCZ has migrated northward bringing southern moisture to the normally arid Sahel region and pushed back the Harmattan winds. The African Easterly Jet (AEJ) is centered at roughly 12°N at the 600 hPa level, between the dry convection area of the heat low and deep convection of the ITCZ. The Saharan air layer (SAL), the dry, northern warm air mass, is shown as ascending in front of the northern edge of the ITCZ. As the SAL is drawn into the oncoming heat low region, it lifts above the cooler, moist air mass transported from the south. This confluence is defined as the inter-tropical front (ITF).

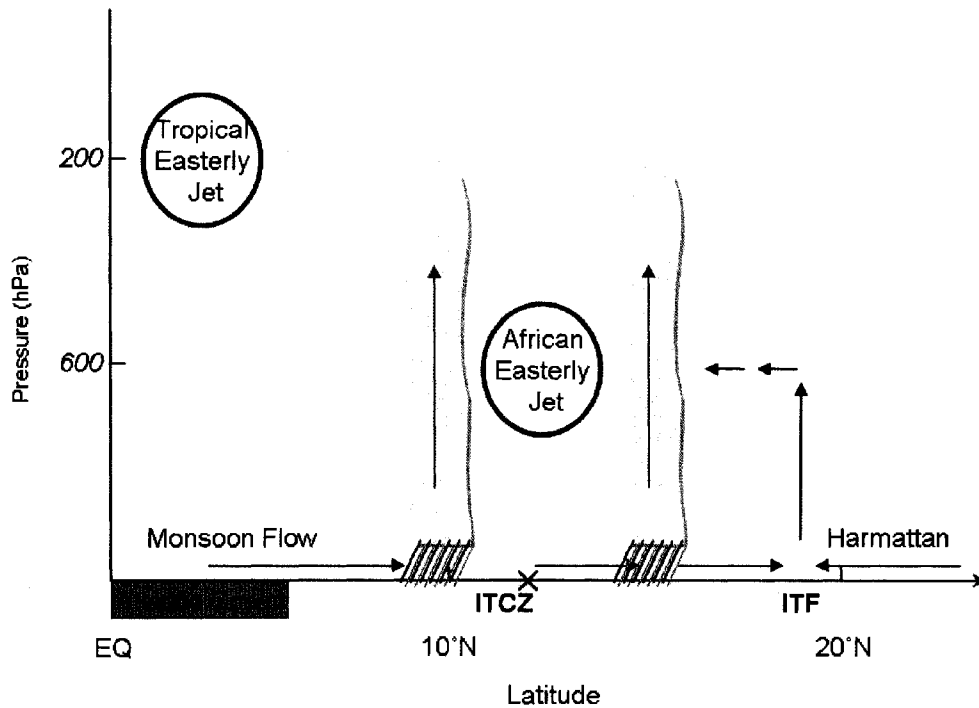


Fig. 5 Schematic of a fully developed West African monsoon, displayed as a latitudinal cross section. The ascending Saharan air layer is shown to flow toward the low created by surface heating located at the ITCZ. Monsoonal flow is shown to be northward and the African Easterly jet forms aloft at the leading edge of the ITCZ (adapted from Hall and Peyrille 2006).

Due to an intrusion of dry air between the ITCZ and ITF (see Fig. 5), this area displays convective inhibition that suppresses sub-MCS scale storms that possess limited size and strength. A large scale, organized event characterized by deep, moist convection may have enough available potential energy to overcome substantial convective inhibition, which is often associated with MCSs (Hall and Peyrille 2006). Sultan and Janicot (2003b) define two distinct phases of the WAM: the “preonset” and the “onset”. The pre-onset marks the migration of the southwesterly winds and ITF past 15°N, while the ITCZ remains south. The onset of the summer monsoon is defined as the abrupt northward shift of the ITCZ from 5°N to 10°N.

The WAM occurs nominally from mid-June through September and has been extensively studied, with observational campaigns employing rain gauge, ground- and satellite- based radar, and IR satellite measurements. It has been established that the average onset of the monsoon is 24 June with a standard deviation of 8 days (Sultan and Janicot 2003b). The WAM generates a large number of SLMCSs, which contribute the majority of observed Sahelian precipitation. The onset criterion mentioned displays interannual variability, which leads to one component of rainfall variability. Grist and Nicholson (2001) summarized that a weaker tropical easterly jet and stronger AEJ characterize a “dry” season, with the opposite true for a “wet” season. These conditions are related to moisture flux and increased vertical shear, with the strength of the AEJ found to be the most dependable characteristic of monsoon strength.

A satellite study of West African squall lines concluded that the first 30 minutes of SLMCSs produce over half of the rainfall that occurs for the duration of the system (Rowell and Milford 1993). Satellite measurements from the GATE experiment suggest that convective rainfall area accounts for only ~10% of the total MCS area coverage (Houze 1993). Past studies have estimated that Sahelian MCS scale storms produce between 80 and 90 % of the annual regional rainfall (Laurent *et al.* 1997; Mathon *et al.* 2002), with the average stratiform rain fraction (of total) at 35% (Schumacher and Houze 2006). EPSAT-Niger raingauge observations (1990-1999) recorded an average of ~360 mm rainfall from 1 July – 15 September (Mathon *et al.* 2002); while Schumacher and Houze (2006) reported that spaceborne radar observations showed average rain accumulation doubles during the monsoon season to $170 \text{ mm}\cdot\text{mo}^{-1}$.

c. African easterly waves

Another unique trait of the WAM is the existence of westward-propagating, synoptic-scale disturbances generated over continental Africa. AEWs exhibit preferential propagation paths consistent with baroclinic wave growth (Berry *et al.* 2007) and commonly include two relative vorticity centers, near the ITF and ITCZ moisture band. It is known that strong shear is exhibited beneath the AEJ (Burpee 1972), where these easterlies aloft are positioned over surface westerlies (Hall and Peyrille 2006).

One theory suggests that increased shear in the AEJ leads to increased convective activity (Matthews 2004), but separating dynamical forcing from the self-organization of convective systems proves difficult. AEW genesis occurs at the site of the AEJ (Hall and Peyrille 2006); where transfer of momentum and energy from the AEJ circulation, through baroclinic and barotropic instability, feeds developing waves. Berry and Thorncroft (2005) posit that AEW formation is a result of large MCS environmental heating causing a perturbation to the wind field in an already unstable atmosphere, which induces barotropically and baroclinically growing AEWs downstream.

Reed *et al.* (1977), Payne and McGarry (1977), and Kilades *et al.* (2006) established that MCS formation preferentially occurs in front of or at the leading edge of an AEW trough, which form over eastern Africa. The exact formation sequence and location is still debated, with recent studies suggesting AEW formation occurs due to convection near 35°E (Berry and Thorncroft 2005; Mekonnen *et al.* 2006). Rowell and Milford (1993), however, suggested that SLMCS formation in the Sahel is enhanced by synoptic forcing in AEWs.

Previous studies have focused on the relationship of SLMCS interaction with AEWs; and SLMCS evolution as a function of propagation across Africa. There is little previous work on how SLMCSs are involved in the evolution of the WAM. This thesis begins addressing this topic by documenting SLMCS occurrence, propagation, and associated rainfall via ground-based radar observations.

d. Radar data quality control

While space-borne measurements allow the study of large spatial scale (i.e. synoptic) occurrences such as AEWs and MCCs, resolution of these instruments for mesoscale and sub-mesoscale phenomena have inherent limitations. Previous studies of the Sahel region dictates that MCS scale events are the most important feature in terms of rainfall during the monsoon season, which also represents the majority of annual rainfall. Land-based radar presents a unique opportunity to study features of mesoscale systems in great detail and to resolve isolated convection, both contributors to annual Sahelian rainfall.

Radars do present inherent challenges, however, in how they sample precipitation systems. Radar echo not associated with the target precipitation system is common, and must be removed before analysis. Anomalous propagation (AP) results when atmospheric refractivity changes with height alter the normal propagation of the electromagnetic signal of the radar beam, resulting in non-weather echo from reflection of the beam off the surface. Weather echo may be range-aliased, which can occur when systems are located outside the unambiguous range of the radar (2nd trip echo). Ground

clutter near the radar is due to topographical features, buildings, and non-meteorological airborne targets, enhanced by superrefraction of the beam normally caused by strong ground inversions. The curvature of the earth causes the ground to “fall away” from the plane parallel to beam propagation and nearly all scans have a small vertical angle applied, therefore ducting and superrefraction only affect the lowest elevation scans (see Fig. 6).

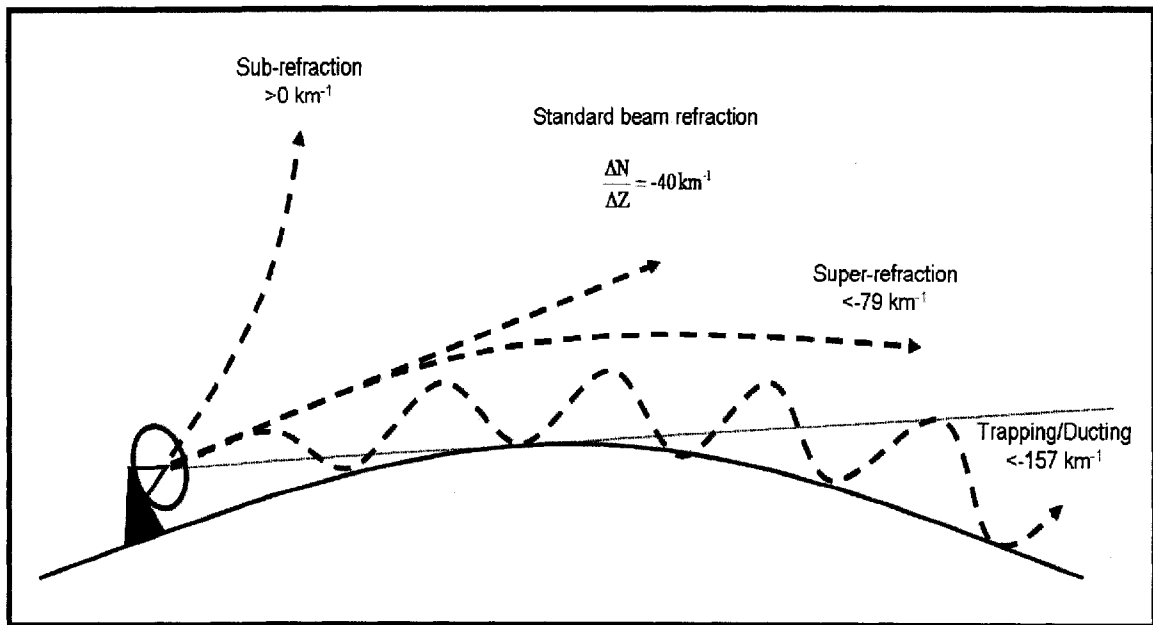


Fig. 6 Diagram of radar beam propagation in various refractivity gradient regimes. It can be seen that superrefraction and ducting occur in the lowest elevation scan angles (modified from Pratte *et al.* 1996).

QC of the data is paramount to prevent misinterpretation of data and provide meaningful rainfall estimates. There are a number of methods, ranging from hardware setup to radar data processing algorithms, used to remove spurious signal both in research datasets and real-time weather data. Use of a specific algorithm is largely dependent

upon processing time available and equipment used in observations. Real-time techniques to remove spurious echo come with the risk of removing meteorological echo, and must be used with caution.

The most difficult corrections to radar data are false signals embedded within real meteorological echo. Removal of ground clutter and AP echo can be initiated during radar installation, real-time or post-collection data processing, or post-collection via a thorough comparison to alternate dataset (Joss and Wessels 1990; Keeler and Passarelli 1990; Pratte *et al.* 1990; Steiner and Smith 2002; Lakshmanan *et al.* 2007). Optimizing radar placement, such as an elevated site, may minimize ground clutter contamination. Thought must also be put into the radar characteristics; wavelength, antenna size, scan strategy, etc. Decision trees based on radar spatial resolution may also be used as a filtering or processing step for collected data. Precipitation and thermodynamic measurements collected or inferred from other data sources, such as IR satellite, rain gauge, lightning data, etc., may be used in a probabilistic approach for prediction of AP echo, providing a base line for processing. A thorough review of the issues discussed above can be found in Steiner and Smith (2002).

Another well studied approach for mitigation of non-meteorological echo is removal in archived data. This approach not only supplies valid observational data for research purposes, but leads to a greater likelihood of the development of AP echo suppression techniques to be implemented in real-time weather analysis. There are multiple approaches that have been explored. Many algorithms have used horizontal and vertical reflectivity gradients (Mueller and Sims 1975; Lee *et al.* 1995; Rosenfeld *et al.*

1995; Fulton *et al.* 1998) or spatial and temporal continuity checks (Smith 1990) for processing archived data. Other approaches focus on Doppler velocity and differential reflectivity fields for removal of spurious echo (Hall *et al.* 1990; Joss and Wessels 1990; Pratte *et al.* 1993). The most recent development has been the advent of probabilistic approaches using multiple parameters as input in fuzzy logic (Kessinger *et al.* 2001) and neural network (Lakshmanan *et al.* 2007) procedures for more sophisticated removal of spurious echo. Though each technique seeks optimal removal of egregious echo, algorithm success is dependent on data characteristics and time frame to produce results. Comparison to alternative datasets and probabilistic approaches are often labor and time intensive. Reflectivity and velocity value and gradient checks may be implemented in real-time observational networks, such as that deployed by the National Weather Service. The QC approach utilized in this study will be discussed in section 3.

3. Methodology

a. Data

SIGMET-IRIS format data from the MIT C-band Doppler radar were saved on-site in real time and archived for later dissemination. Multiple scan techniques were employed to process radar information. The dataset included volume, survey, and Range Height Indicator (RHI) scans; only the volume scan was used for this research. A full 360° (with radar at the center), three-dimensional field of view was attained for multiple distances by adjusting the pulse repetition frequency (PRF), which is a measure of pulses per second and effectively controls the unambiguous scan range given the inverse dependence on PRF (survey scans). A vertical profile of the atmosphere was produced by vertical scan steps along a constant radial (RHI). Reflectivity volume scans (with fixed PRF), composed of 15 elevation angle sweeps, were collected at ten minute intervals (characterized in Table 2). Over 11 250 volumes from the observational period underwent conversion processing and analysis.

Table 2. Software packages utilized to process MIT radar data for the 2006 AMMA project.

Elevation angles(degrees)	0.5, 1.3, 2, 2.8, 3.9, 4.9, 6.2, 7.5, 9.1, 11.1, 13.5, 16.4, 19.9, 24.1, 29.2
Maximum unambiguous range	149 km
PRF	950 Hz
Bin spacing	250 m

Iterative examination of reflectivity fields throughout the lowest 3 km above ground level (AGL) revealed no substantial difference in the occurrence of non-meteorological echo; therefore, all ensuing analysis was performed at a constant 1 km altitude. Analysis at low altitude allowed rainfall estimates of precipitation reasonably

close to the surface, enhancing the comparison to surface-based rain measurements. Unambiguous radar reflectivity range was 150 km, though only values within a 130 km radius were used in calculations. Outside of this calculation range, beam expansion resulted in significantly lower resolution of convective elements.

b. Processing raw data

SIGMET-IRIS radar data, a proprietary format, were first converted to universal format (UF; Barnes 1980; Dolan and Rutledge 2007), a standardized radar data format that maintains the natural coordinates of the radar, via a software package developed as part of the ground validation program at the Tropical Rainfall Measurement Mission (TRMM) Satellite Validation Office (TSVO) at the National Aeronautics and Space Administration (NASA) Goddard Space Flight Center (GSFC). The package includes Radar Software Library (RSL) RSL_nsig_to_radar and RSL_radar_to_uf functions, available from the TSVO Web site (http://trmm-fc.gsfc.nasa.gov/trmm_gv/). The RSL algorithm distinguishes between full volume scans, which are retained, and RHI or survey scans that are discarded. Conversion to UF is necessary for processing with further software packages, and represents an accessible format easily read by most radar processing packages and analysis programs in commonly used languages (e.g. C, FORTRAN, or Interactive Data Language (IDL)).

An alternate software program, called the Ground Validation System (GVS), was used for data QC purposes. This TSVO software, also freely distributed online, contains capabilities of a complete processing package with three components, file conversion and

QC product (Level 1; 1C-51) and two precipitation characterization products (Levels 2 and 3). Only Level 1 was employed to produce QCed, or corrected, reflectivity scans, based on an algorithm derived from Rosenfeld *et al.* (1995). Removal of contamination by non-meteorological echo and AP is covered in more detail in section 3d.

Next, the “REORDER” software package (in FORTRAN) developed at the National Center for Atmospheric Research, processed UF files to network Common Data Form (CDF) file format, a standardized, commonly used data format (Mohr *et al.* 1986). Polar coordinate-oriented raw data were interpolated to a Cartesian coordinate system representative of the geographic sample area, with 1 km horizontal and vertical spacing using a Cressman weighting scheme (Cressman 1959; Daley 1991). Delta-azimuth, -elevation and -range components of the radius of influence are employed during conversion, which results in variable radii, rather than fixed delta-x, -y, and -z radii to optimize the interpolation accounting for the increasing distance between data rays with increasing range. Figure 7 shows the sampling volume used for Cartesian transformation of radar data from polar scan coordinates (Mohr and Vaughn 1979; Mohr *et al.* 1986); note the constant change in azimuthal, elevation, and range steps.

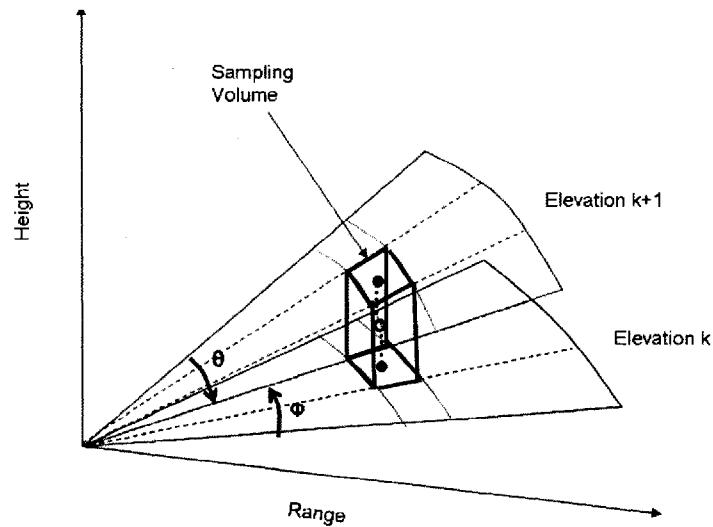


Fig. 7 Illustration of sampling volume used for Cartesian transformation of radar data from polar scan coordinates. Solid dots are projection points, while the open dot represents a Cartesian grid location on consecutive elevation scan planes, k and $k + 1$. The angle along azimuth is θ , while Φ is the elevation angle (modified from Mohr *et al.* 1986).

Transformation can result in smoothing of data at high altitudes (Dolan and Rutledge 2007), resulting in the coarse resolution aloft. This study is interested in ground precipitation and therefore disregard the outermost 20 km of radial reflectivity data where natural beam propagation is elevated AGL and sample volume has poor resolution due to radar beam divergence. Multiple data fields are available for retention in CDF file format, including the raw reflectivity data and QCed, or corrected reflectivity data. Doppler radial velocity data may also be included, but was not used for this study.

Finally, a program written in ITT Visual Information Solutions, Inc. IDL was used to process CDF files into image formats (gif, tiff, ps). IDL is a powerful visualization software package with the ability to process multiple file types and output high quality images. The algorithm assigned the interpolated Cartesian grid data onto a map image. The resulting image files were merged into animations used for event

classification and iterative QC measures. Software operation procedures can be found in Table 3, with an overview of the procedure flow for radar data processing found in Fig. 8.

Table 3. Software packages utilized.

	Input Data →	Software →	Output Data
Initial analysis	IRIS (raw)	RSL	UF
	UF	REORDER	CDF
	CDF	Cappi_vol	gifs
Quality control analysis	IRIS (raw)	GVS level 1	UF
	UF	REORDER	CDF
	CDF	Cappi_vol	gifs, plots, data files

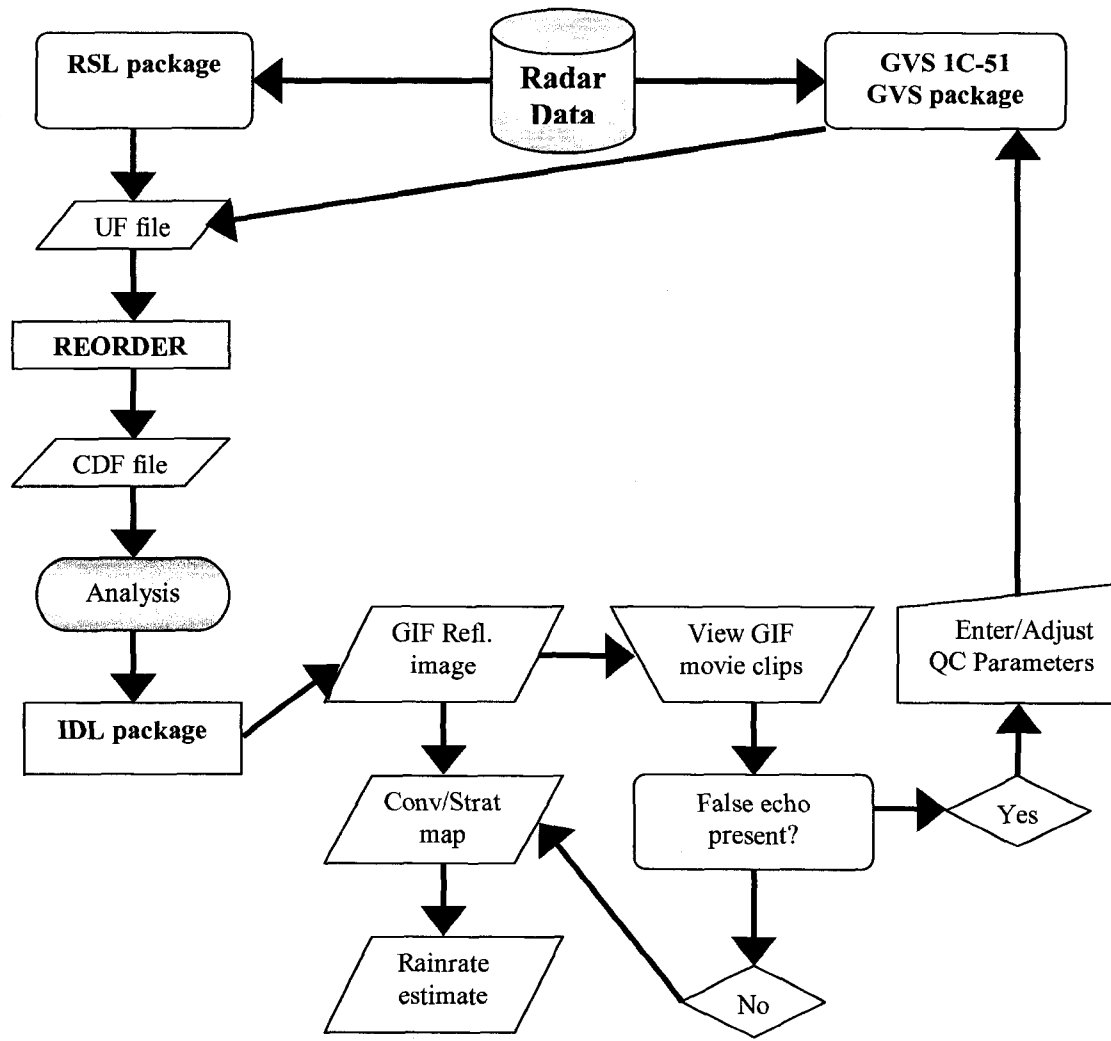


Fig. 8 Flowchart depicting the order of software operation according to the decision tree structure indicated.

c. Data classification (qualitative)

Classification techniques for cloud system size and strength have been developed in the past according to the scope of study. Rickenbach and Rutledge (1998) used a four-event categorical system that included MCS and sub-MCS horizontal dimension scales as the two general classes, and subclasses that denote whether the convective cells displayed linear organization, referred to as linear and non-linear. A simplified version of the classification system was used for this study, in which systems were classified as either MCS or sub-MCS. These categories arise as a function of spatial scale according to the definition provided in Section 2 from Houze (1993); where MCS-scale events have horizontal scale ≥ 100 km and sub-MCS scale events horizontal scale < 100 km. Though not pertinent for this study, MCS-scale events were designated as MCS or SLMCS, depending on amount of linear organization; and sub-MCS scale events were given such designations as isolated convection and scattered convection.

Time-lapse animations of reflectivity scans allowed the manual construction of an event log, in which each scan volume was categorized according to classification of events present. Radar reflectivity images allow the viewer to classify sub-MCS and MCS-scale events (see Fig. 9).

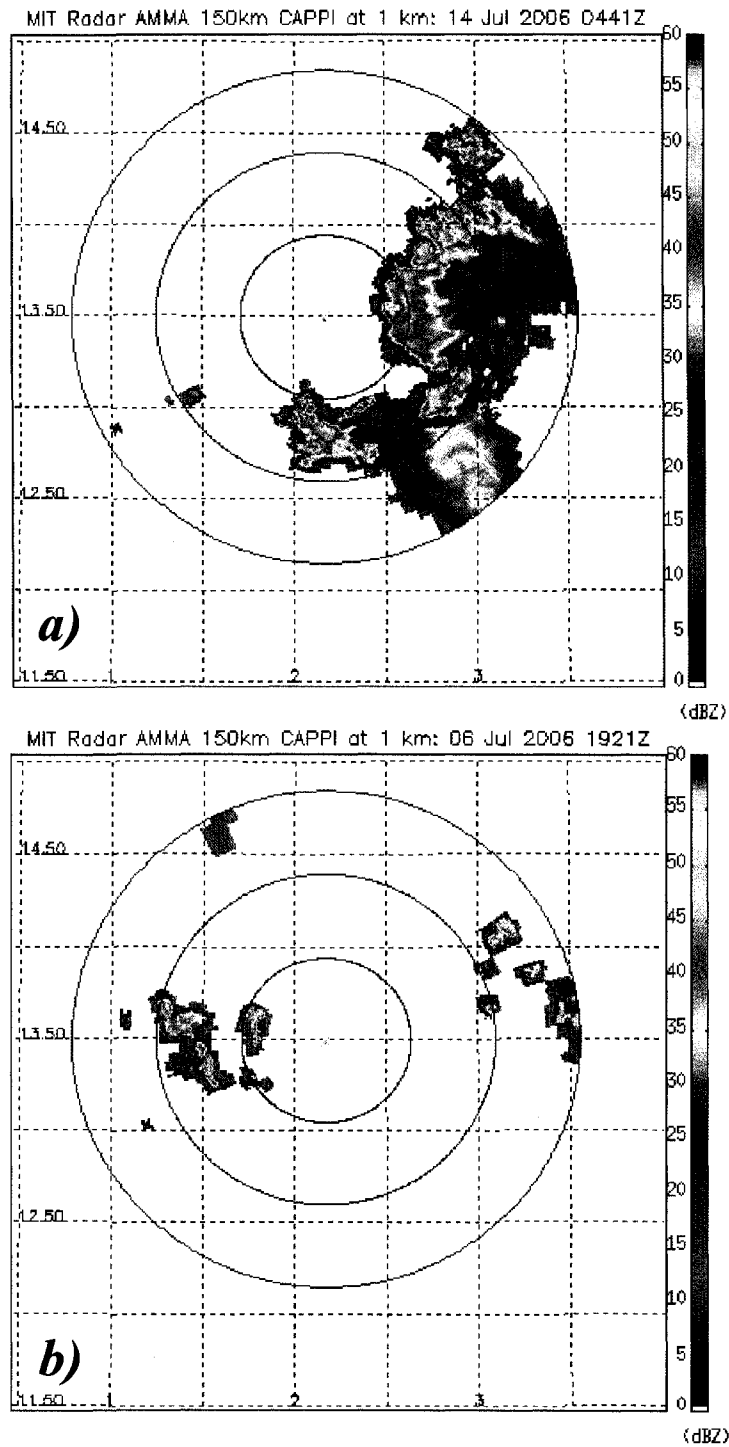


Fig. 9 Constant altitude plan position indicator radar reflectivity maps at 1 km height, containing a) a MCS scale system and b) a sub-MCS scale system, occurring on 14 July and 6 July 2006, respectively. Radar range rings are given every 50 km.

The majority of MCSs are easily identified, but there is a degree of subjectivity present. A limited number of cases (<5) do arise when only the far edge of a SLMCS is visible in the limited viewing area of the radar; designation is then somewhat subjective which accounts for differences that can arise from study to study.

Tables 4 and 5 show a monthly distribution and occurrence time, respectively, of MCS events, where SLMCS occurrences are a large subset of MCS events.

Table 4. Monthly distribution of and total MCS-scale events for the 2006 West African monsoon season.

Month	Number of events	
	MCS	SLMCS
July	12	9
August	14	10
September	11	5
Total	37	24

Note that Niamey local time (LT) is Universal Coordinated Time (UTC) + 1 hour. End times were defined as the time when convective and stratiform precipitation regions propagated out of the scan area or dissipated sufficiently. Sub-MCS scale events were a result of localized convection forming in the scan region, typically diurnally heat-driven.

MCS-scale events generally entered the radar view field from the east and propagated in a westward direction, though northwestward and southwestward propagation were also observed. While strengthening and decaying were sometimes evident, no MCS formation was observed within the radar area. There were a total of 39 MCS scale events that occurred throughout the WAM season, approximately 72% of which were designated as SLMCSs. Generally MCSs appeared as strong convective cores, often in a well-organized leading line, with trailing stratiform region behind (Fig.

10). Stratiform precipitation often formed as convective cells decayed and persisted well after convection moved through the sample region.

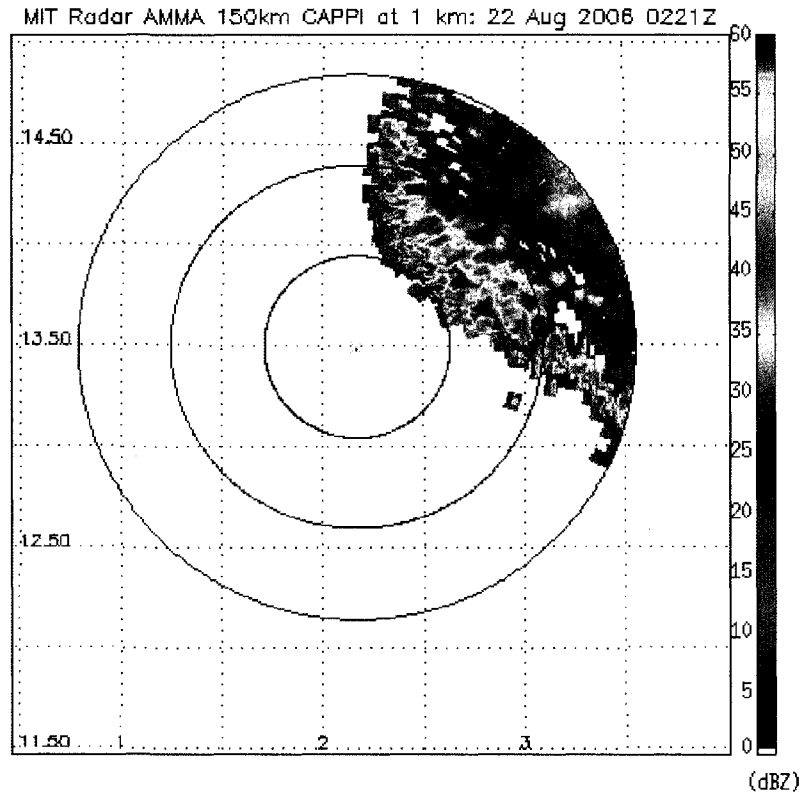


Fig. 10 Observed squall line mesoscale convective system on 22 August 2006, representative of many MCS scale systems observed over the course of this study. This particular system exhibited a classic bow structure of the leading convective cores, with massive trailing stratiform precipitation. Radar range rings are given every 50 km.

Table 5. MCS event times for the 2006 West African monsoon season. Niamey, Niger local time is UTC + 1hr.

Month	Begin		End	
	Date	Time (UTC)	Date	Time (UTC)
July	05	1621	05	2331
	06	1511	07	0721
	08	1351	09	1511
	11	1331	12	0031
	13	2151	14	1021
	14	2211	15	1331
	17	0411	17	1311
	19	0211	19	1221
	22	0311	22	1621
	24	2051	25	1931
	25	1941	26	0811
31	0631	31	1651	
August	03	1101	04	0651
	06	0321	06	1801
	07	1051	08	0131
	08	0941	08	2201
	11	0031	11	1031
	14	0641	14	1841
	17	0431	17	1101
	18	0131	18	1541
	22	0011	23	0401
	24	1601	25	0311
	26	1041	26	1831
	28	0001	28	1551
	30	0531	30	1241
30	2351	31	0251	
September	03	1101	03	1901
	03	2141	04	0051
	05	0701	05	1731
	08	0151	08	1901
	08	2341	09	0851
	10	1301	11	0901
	12	1301	12	1811
	14	0511	14	1031
	18	1921	19	0741
	21	0121	21	1501
	23	2211	24	1551

One unique MCS event occurred 9 September between 0000-0900 LT, where widespread stratiform was present throughout the observable domain (Fig. 11). Contiguous, low order precipitation was present across a wide scan area, with no discernable organization. This event was quite similar in structure, evolution, and diurnal timing to nocturnal stratiform systems in western Amazonia (Brazil), described in Rickenbach (2004). There was no evidence of local convection embedded with the cloud cover, though the horizontal dimension was adequate to meet requirements of the MCS classification. This was the only occurrence of such a system.

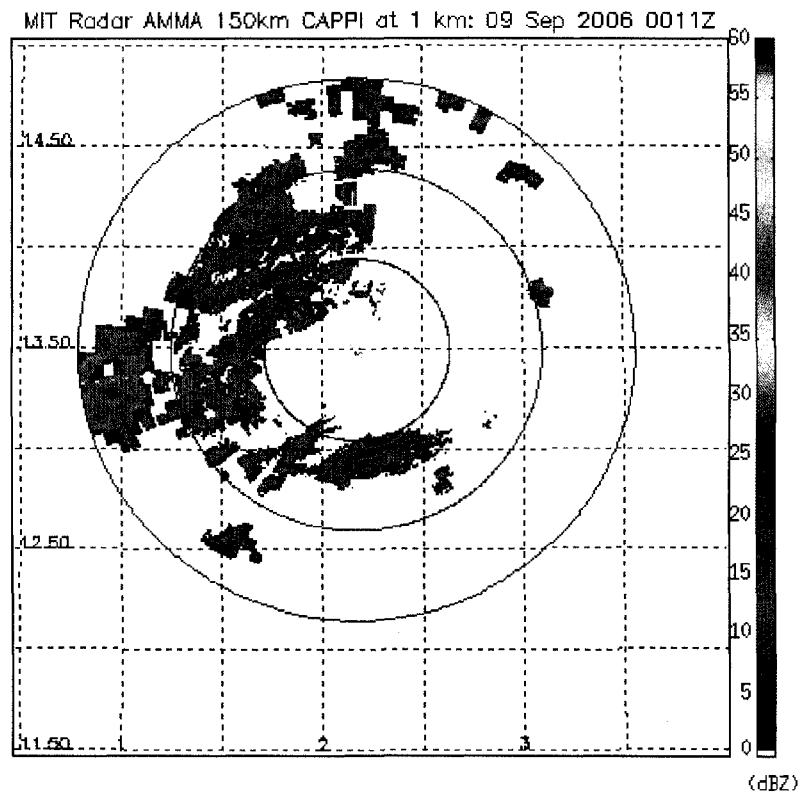


Fig. 11 A unique stratiform precipitation event that occurred 9 September 2006. There was no preceding or subsequent convective system to account for widespread stratiform observed. Radar range rings are given every 50 km.

d. Data quality control (quantitative)

General information regarding the displayed reflectivity data was attained through classification of the raw data, including duration and occurrence time of events, propagation direction, and visual estimates of portion of the total system that was acquired in the sample region. To attain useful quantitative results, egregious echo must be removed, leaving only the meteorological echo of interest. The QC algorithm in the component of GVS (1C51) was applied, which is controlled by eight adjustable parameters; three echo height thresholds (H1, H2, and H3), and five radar reflectivity thresholds (Z0, Z1, Z2, Z3, and dBZ_{noise}) that provide a logical decision tree for removal of AP (Kulie *et al.* 1999; Marks *et al.* 2000; Robinson *et al.* 2001). The parameters are utilized to help distinguish between typical characteristics of anomalous echo and those of echo associated with various types of rain producing clouds. Echo heights and depths along with reflectivity gradients are evaluated to ensure reasonable precipitating features are kept, while questionable echo is discarded. AP is manifested as shallow radar echo that appears as a radial spike or speckle (noise) pattern in the radar field, while meteorological echo displays substantial vertical echo structure. Parameter values are site-specific, dependent upon local characteristics, such as topography and climatological profiles of moisture and temperature in the lower atmosphere. Use of values optimized for another location would likely result in inadequate QC results.

The algorithm applies a corrective filter to the reflectivity data by way of ~1x1 km masks, resulting in echo suppression according to user-specified parameters discussed below. Uncorrected reflectivity fields can be attained by subtracting the mask from the

corrected reflectivity field. This algorithm represents a modified approach developed by Rosenfeld *et al.* (1995), where the following radar data conditions are considered for decision tree input:

$$Z_{top} < H3 \text{ or } Z_{max}(3km) \leq Z1; \text{ and } Z_{max}(H1) \leq Z3, \quad (1)$$

$$Z_{top} < H2, \quad (2)$$

$$Z_{max}(1.5km) \leq Z0, \quad (3)$$

$$\{ Z > dBZ_{noise} \text{ and } Z < Z2 \} \text{ in the lowest tilt.} \quad (4)$$

where Z_{top} represents echo top height, with general radar noise defined by the dBZ_{noise} threshold, and $Z_{max}(h)$ is a maximum reflectivity value at a specified height, h . Once any condition put forth in Eq. 1-4 is satisfied, the reflectivity value is rejected.

Equation 1 filters shallow noise and some ground clutter. Suppression is accomplished if Z_{top} does not exceed the user-specified height parameter (H3); or the reflectivity value at 3 km altitude is less than a user-specified reflectivity parameter (Z1). In addition to the previous conditions, if the maximum reflectivity at the first user-specified height threshold (H1) is less than parameter reflectivity threshold (Z3), the echo is masked. These conditions remove spurious echo that is manifested in the lowest scan levels (and hence heights) and requires that a level of vertical development is required to maintain precipitating clouds.

Equation 2 establishes a minimum level for echo top height by requiring that Z_{top} be higher than a parameterized height threshold (H2). Any low clouds (stratus) will be masked according to this condition. If Z_{max} at 1.5 km height is less than a minimum

threshold (Z_0), the reflectivity values are filtered, according to Eq. 3. This enacts a minimum reflectivity at 1.5 km altitude to ensure echo present is precipitation.

Finally, the lowest tilt is checked. If the reflectivity is greater than the $\text{dBZ}_{\text{noise}}$ threshold and is not greater than parameterized threshold (Z_2), reflectivity data will be suppressed. Ground clutter, often manifested as low- to mid-level noise, is largely removed from this condition. Upon satisfaction of any criterion specified by Eqs. 1-4, echoes are masked up to a level of $H_3 + 1$ km and height checks are only performed when the top of the examined volume scan is greater than echo top height. Reflectivity values are rejected when all conditions listed are fulfilled.

Ground clutter is manifested as weak echo that is normally confined to the lowest tilt and therefore will be removed largely by a radar noise threshold. If a stronger signal is apparent from a stationary target, it will likely be confined to low tilt levels and thus be filtered. Weak 2nd trip and clear air echoes are effectively removed with the algorithm above; however, strong 2nd trip echo proves more difficult to differentiate from a meteorological signal, especially when embedded within real precipitation. Approaching MCSs often produced large 2nd trip echo signals, removed by maximizing filter settings, in essence clearing all reflectivity from the scan. Any light precipitation preceding a MCS was also filtered. It is important to note types of meteorological events that are lost during the QC process. Some meteorological echo, such as gust fronts and light precipitation, were filtered via the algorithm. This thesis is interested in general system morphology and relative rainfall, therefore the filtering was appropriate to ensure optimum performance for the scope of this study.

The NASA GSFC TSVO graciously provided guidance on a small number of test files from the Niamey radar data set, offering their enormous amount of experience of radar data QC in the TRMM ground validation program (Gebremichael *et al.* 2006). A parameter file with variable threshold parameter values dependent upon scan time was constructed to automate the QC process over the entire dataset based on operator review of echo situation in each scan. Default algorithm parameters were established to apply to the entire data set, except for certain meteorological situations as described later. Parameter sets extracted for individual cases, e.g. 2nd trip echo preceding a MCS system approach into the radar view area, were applied to similar events throughout the dataset (see Table 6) and provide processing schemes for removal of spurious signal by atmospheric phenomena and ground and AP echo.

Table 6. GVS Level 1 quality control software (1C51) parameters resolved for quality control algorithm of the 2006 AMMA radar dataset.

Situation	H1	H2	H3	Z0	Z1	Z2	Z3	dBZ _{noise}
	(km)			(dBZ)				
Local convection	2.0	3.0	1.5	10.0	10.0	10.0	15.0	0.0
Default	3.5	3.5	4.0	16.0	18.0	18.0	28.0	0.0
AP	5.0	4.0	6.0	18.0	22.0	20.0	30.0	15.0
Complete echo removal	7.0	7.0	7.0	77.0	77.0	77.0	77.0	0.0

Default values were applied to all cases unless the parameter file indicated use of a select parameter scheme. The default values were based on those used at a separate AMMA radar location in Senegal, Africa and previous GSFC experience of land-based, continental radar systems. These values often proved to be the best filter settings when

SLMCSs propagated through the scan area. Corrected scans were compared with raw data files by visual inspection to judge removal of egregious echo while meteorological echo remained largely intact. Analysis of SLMCS cases showed less contamination in the radar scan range than other events mainly due to the presence of strong reflectivity (deep convection) signals in the scan and the substantial area coverage associated with SLMCSs.

During local convection less low-level noise was apparent, therefore parameter values were minimized to allow the maximum amount of precipitation to be unfiltered. Default values were produced through the iterative optimization mentioned above; which can be found in Table 6, where each successive row represents a more stringent set of values for echo removal. Height and reflectivity thresholds were increased to retain wide spread stratiform event information, which would be lost with more stringent parameter values. AP echo proved more difficult to remove as often the associated reflectivity values were higher than those filtered through the default settings and were often present preceding and after a MCS system was observed in the radar range. All echo was removed from a scan area by applying the final set of parameter values. This case was used for instances of wide-spread egregious echo; such as widespread speckle generated by a morning temperature inversion, at a time when no meteorological event occurred, which were verified by operator logs and satellite imagery.

The process shown in Table 3 was employed once again to produce output data and images. The filtering process was iterated to provide optimum results in general and on a case-by-case basis for the removal of non-meteorological echo, while allowing

precipitation echo to remain largely unchanged. Visual inspection of the raw reflectivity images against images of iterative corrected attempts with adjusted algorithm parameters, were used to judge spurious echo removal. Exclusion of obvious non-meteorological echo was mandatory, along with weather echo aliasing. Minimum loss in meteorological echo, e.g. preserving maximum stratiform echo coverage, was sought. Figure 12 demonstrates a) raw data, b) GSFC results, and c) study results of the QC process; note there is a general concurrence of precipitation features. Nearly all clutter near the radar and 2nd trip echo was removed by parameters used by both GSFC and those selected for this study. The light echo at the far left (western) edge was retained by the San Jose State University (SJSU) parameter set (Fig. 12c), while largely removed by the GSFC parameters (Fig. 12b). Though this echo exhibited radial reflectivity patterns similar to some AP occurrences, it was deemed to be meteorological echo due to the non-uniform nature of the radial reflectivity and the presence of a large noise level within this particular file, often associated with greater convective activity in the scan field. Lower values of reflectivity were retained as the scan range limit was approached, allowing weak echo to remain.

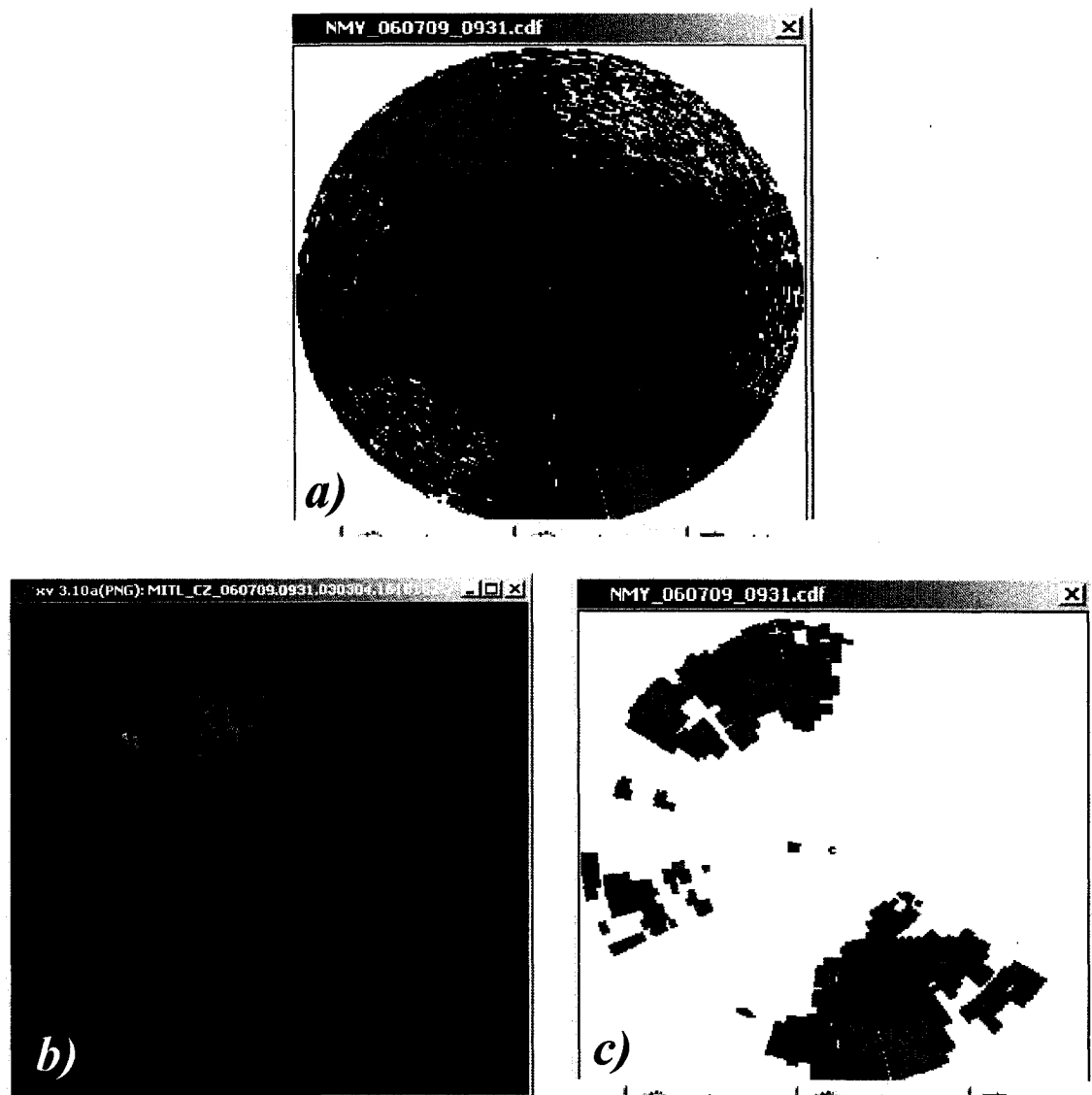


Fig. 12 Radar echo maps showing a sample of a) no quality control filter, b) region-specific default parameters provided by GSFC, and c) region-specific special case parameters applied for spurious radar echo removal resolved by SJSU.

The results of this study consistently show greater precipitation coverage at longer range, due to refinements in applied QC parameters chosen from interpretation of results via the iterative process previously discussed. There is a small tilt to the radar beam (0.5°), resulting in increased elevation as the beam propagates away from the radar.

Information close to the radar comes from the same elevation angle, while multiple elevation angles are needed to construct 1 km Constant Altitude Plan Position Indicators (CAPPIs) at distant ranges, resulting in lower overall resolution of features near maximum range. The QC algorithm tends to retain a greater amount of echo at large distances (> 100 km) due to decreased data resolution that limits the echo that may be discarded at low levels closer to the radar.

Sources of clutter also included morning temperature inversions, which result in the radar beam bending toward the ground; and range aliasing preceding the approach and following the propagation of a MCS. Inversion clutter was removed by application of an increased reflectivity threshold value filter during morning hours. False convection was verified with parallel analysis of infrared (IR) satellite images and removed by more stringent parameter criteria. One well known caveat of the 1C51 software is the failure of the algorithm when spurious echo is embedded in real precipitation echo. Removal often requires rejection of real precipitation echo, which can result in an underestimate of rainfall in the scan region. This spurious echo was commonly observed in the trailing stratiform components of large SLMCSs propagating through the scan region. Therefore, there was a need to sacrifice some stratiform coverage to eliminate artificial convection. Most egregious anomalies remaining in the data were, however, removed during processing by the situation-specific parameter filtering discussed (Fig. 13).

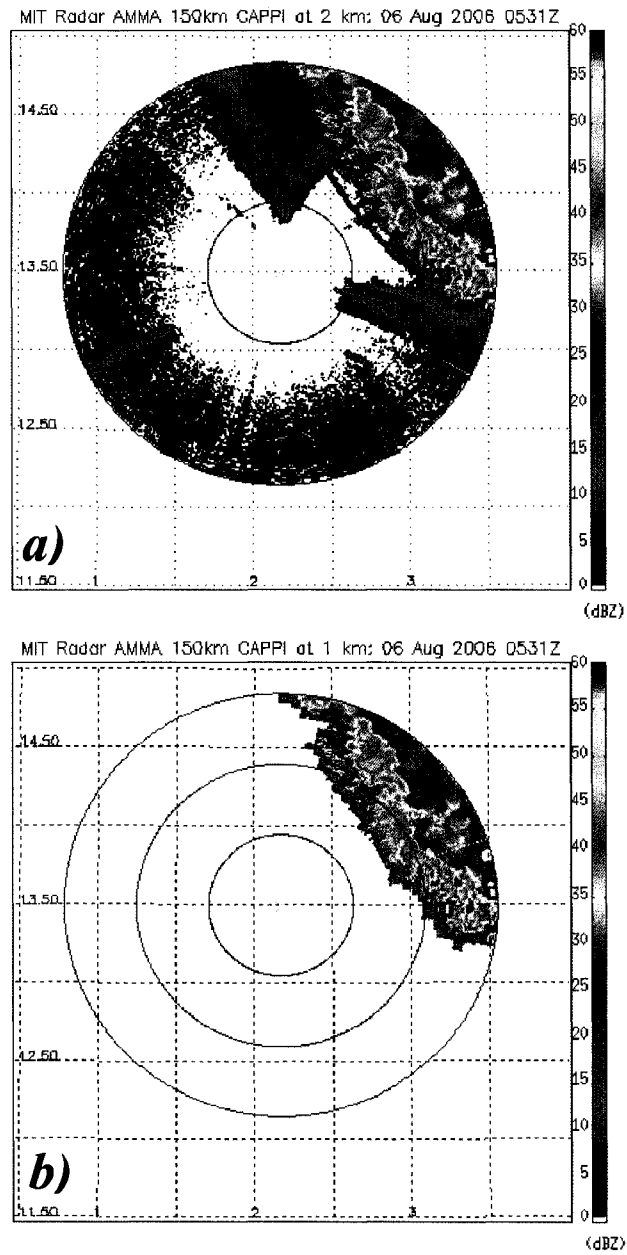


Fig. 13 Radar reflectivity data displayed as a) raw data and b) quality controlled data. Spurious echo was removed via quality control efforts employing GVS 1C51 software. Radar range rings are given every 50 km.

e. Rainfall estimation and convective-stratiform partitioning

After QC of the dataset, reflectivity data was used to estimate rainfall. Sauvageot and Lacaux (1995) analyzed drop size distribution (DSD) shape with respect to rainfall rates from disdrometer data obtained for several locations in Africa and France, with continental African sites at Niamey, Niger and Boyélé, Congo. Averaged DSDs were used to remove random variations inherent in the instantaneous DSD measurement due to such complications as kinematic effect on drop trajectory. A lognormal distribution was used to represent averaged drop spectra, where concentration of small drops was very low. Reflectivity - rainfall rates (Z-Rs) were obtained through direct regression of raw disdrometer data at a one minute resolution. The Z-R used for this study was:

$$Z = 364R^{1.36} \quad (5)$$

The general approach of Rickenbach and Rutledge (1998) was followed for convective-stratiform partitioning and may be consulted for a more detailed account of the approach used; a general overview is provided here. Identification of convective and stratiform regions would ideally come from direct measurements of vertical air motion magnitudes (Houze 1993), with strong vertical updrafts associated with convective cells. These data are not available for convection in the radar range during AMMA; and therefore an indirect method is required to identify convective and stratiform regions.

Assessment of spatial radar reflectivity gradients allows the isolation of intense, horizontally variable precipitation from weaker, extensive precipitation indicative of convective and stratiform rain, respectively (Steiner *et al.* 1995; Rickenbach and Rutledge 1998). Criteria for this convective rain-identifying technique are intensity and

peakedness, a local reflectivity maximum of specified strength. The intensity criterion was satisfied when reflectivity > 40 dBZ, implying convective rain. Local maxima less than the 40 dBZ threshold may also be considered convective if a peakedness criterion is met. The value must exceed the mean reflectivity in an 11 km circular radius about the point by 4.5 dBZ, which equates roughly to a factor of two in rainfall rate. Upon convective cell designation, a circular cell about the point, with radius between 1 and 5 km, are considered convective. All other reflectivities are considered stratiform precipitation. A SLMCS case is shown in Fig. 14, with the reflectivity map of the QCed radar data (Fig. 14a), and the accompanying convective-stratiform partition map generated through the algorithm discussed (Fig. 14b). The linear, leading structure of strong convection can be seen (red and yellow in Fig. 14b) with a substantial trailing stratiform component (blue in Fig. 14b). There is no apparent echo beyond 130 km, which is a product of the partitioning algorithm that does not extend beyond this range, due to the low resolution of data and the radial differencing calculations employed. Comparison to the reflectivity map shows that the partitioning algorithm effectively separates the components.

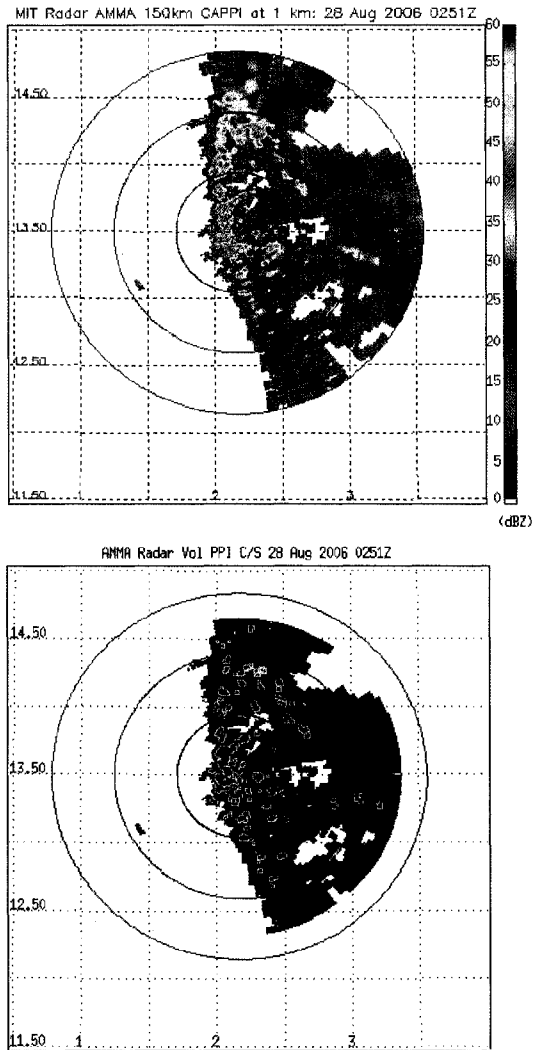


Fig. 14 A large squall line mesoscale convective system event plotted as a) reflectivity and b) convective-stratiform component map. The reflectivity map is generated from corrected radar data, while the convective-stratiform map is resultant from a partitioning algorithm operating on corrected radar data. A linear, strong leading convective edge is apparent with a large trailing stratiform component. The color gradation in a) is related to reflectivity value (dBZ), while in b) red and yellow represent areas of convection and blue show areas of stratiform.

4. Results

a. QC performance

Default QC parameters effectively erased spurious echo such as ground clutter and weak 2nd trip echo. Figure 15 shows examples of a) weak and b) strong ground clutter and clear air signals that are effectively removed (Figs. 15c-d) by application of default parameters in the QC algorithm. Morning inversions, more prevalent in September (Fig. 15c), were also efficiently removed by this basic default state. Given that these egregious signals are present at the lowest scan levels; vertical extent of the contamination up to 3.5 km is unlikely to occur. Reflectivity values are relatively weak when compared to convective reflectivities, even in the case of Fig. 15b, which shows the strong noise case. The maximum reflectivities are generally no more than 10 dBZ, while the default parameters will filter signal less than 16 dBZ.

As a radar pulse propagates away from the source, beam divergence due to non-zero beamwidth results in a larger scan area. If a storm is detected outside of the unambiguous radar range, the signal will be aliased within the scan area (a function of the wave characteristics of the radar pulse). The aliased signal will appear in a volume smaller than that sampled and will therefore appear as an elongated reflectivity signal along the radius of displayed scan area. This is referred to as 2nd trip echo, and is shown in Fig. 16. An example of weak 2nd trip echo is shown in Fig. 16a where only noise is present with no precipitation, while Fig. 16b shows 2nd trip echo preceding an approaching MCS, with precipitation signal beginning to appear near 3.5°E, 13.25°N. This spurious signal may also be embedded within and adjacent to precipitation signal as

seen in Fig. 16c. Default parameters, as discussed above, often remove weak 2nd trip signal (Fig. 16d), but are unable to remove stronger signal.

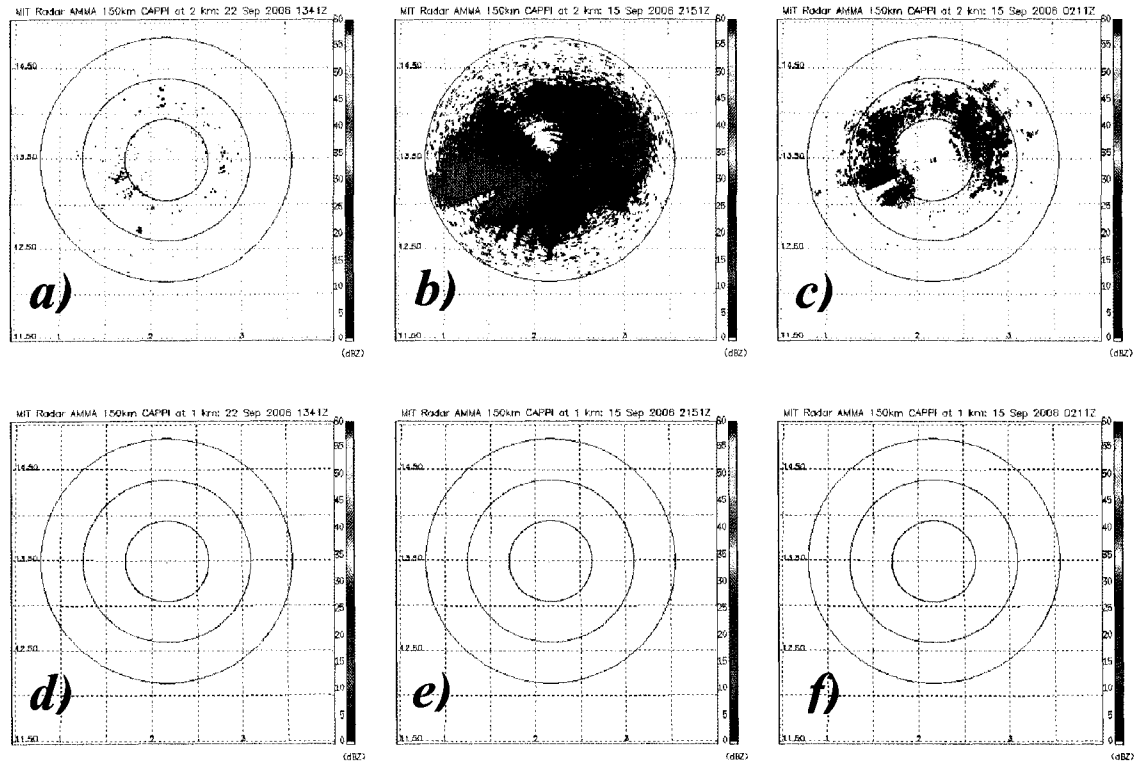


Fig. 15 Examples of before (a-c) and after (d-f) quality control of radar reflectivity scans containing a) weak noise, b) strong noise, and c) noise caused by morning inversions by the GVS 1C51 algorithm. Radar range rings are given every 50 km.

The AP scheme in Table 6 is applied for removal of stronger 2nd trip echo preceding and adjacent to precipitation signal. Figures 16e-f show the remaining reflectivity after QC processing, in both cases the convective signal is retained, with a small portion of 2nd trip echo remaining at the southern edge of the convective signal centered near 1.8°E, 13.5°N. It is evident that some stratiform echo was sacrificed (Fig. 16f), which caused artificial gaps in the echo cover. Some loss of MCS stratiform may

occur due to the condition expressed in Eq. 4, which will filter signal between 15-20 dBZ at the lowest tilt angle.

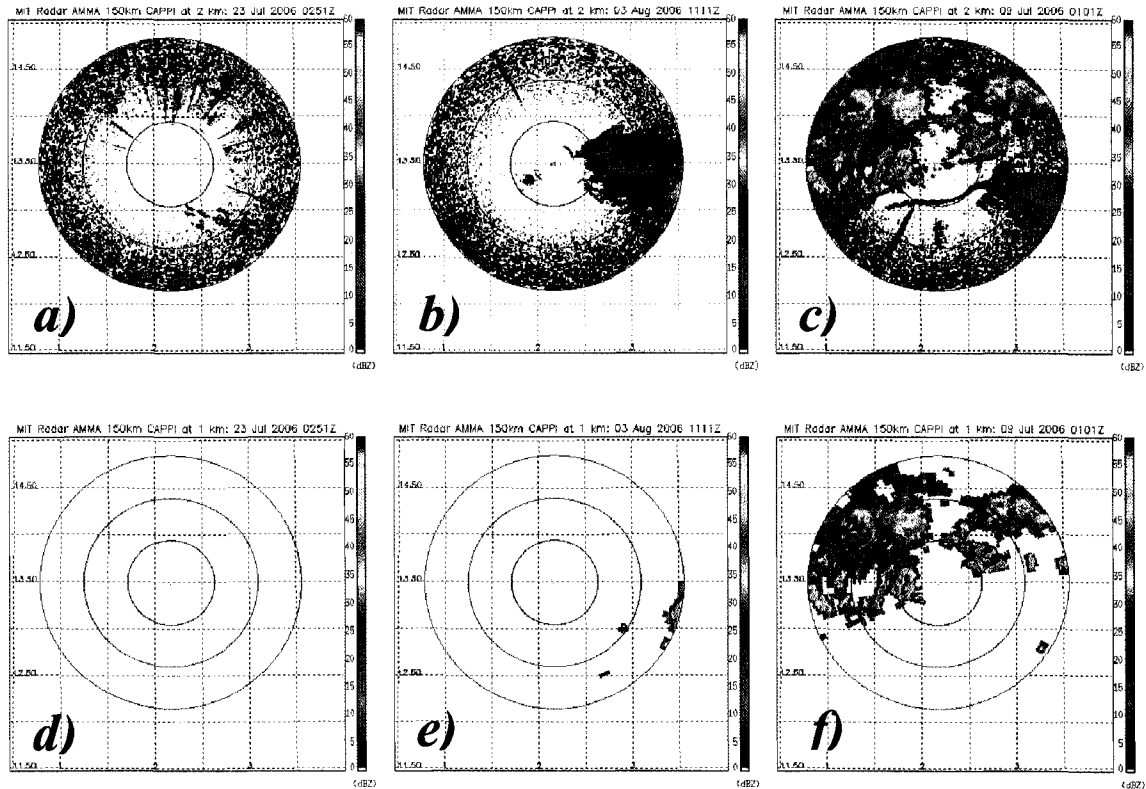


Fig. 16 Examples of before (a-c) and after (d-f) quality control of radar reflectivity scans containing 2nd trip echo a) in pure noise, b) preceding MCS approach, and c) embedded in a precipitation signal by the GVS 1C51 algorithm. Radar range rings are given every 50 km.

Isolated convection is composed of small, individual convective cores (Fig. 17a) often formed from local thermal forcing. These storms have a short lifetime and normally possess relatively small amounts of stratiform echo compared to MCSs. Multiple occurrences in the radar scan area constitute scattered convection (Fig. 17b). Default and AP parameter schemes work equally well to QC a file. The decision of which scheme to use is dependent upon the level of noise present in the scan. Note that

in Fig. 17d, a small piece of non-meteorological echo remains near 1.75°E, 14.7°N (northeastern domain at 140 km range) due to a relatively strong reflectivity signal of ~35 dBZ. Applying more stringent QC parameters in this case would result in diminishing the meteorological echo in the scans, and begin to sacrifice convective precipitation signal. The non-meteorological echo was diminished to a small area with reflectivity that is too weak for convection, and the precipitation contribution from this echo is sufficiently small enough to warrant no further removal iterations.

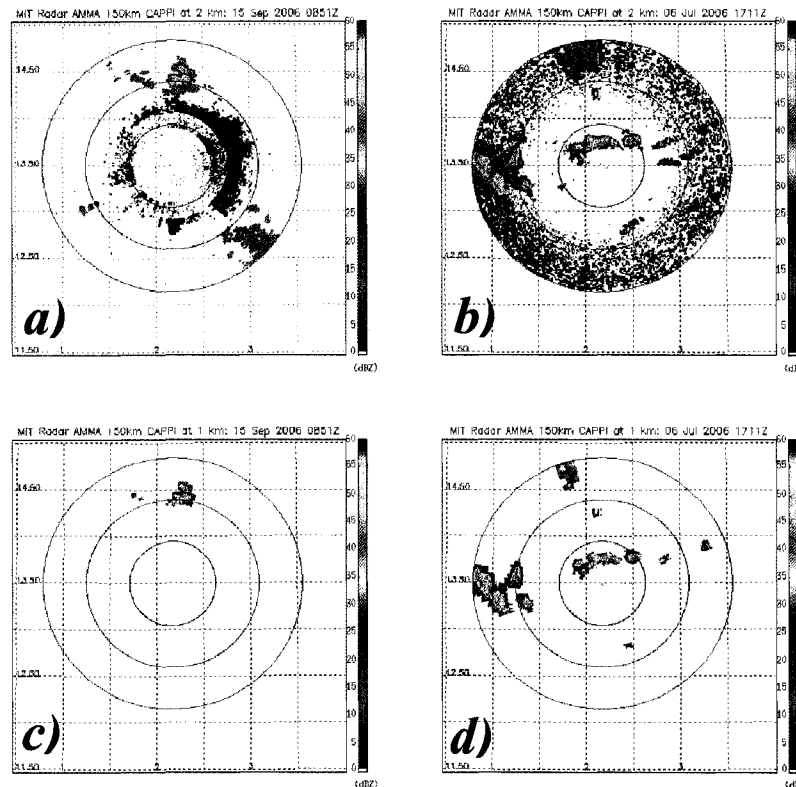


Fig. 17 Examples of before (a-b) and after (c-d) quality control of radar reflectivity scans containing a) isolated and b) scattered convection by the GVS 1C51 algorithm. Radar range rings are given every 50 km.

Retention of MCS precipitation was an important aspect of this study. A MCS covering nearly one quadrant of the radar scan area is examined in Fig. 18a, while another MCS system that occupies almost the entire scan region is shown in Fig. 18b. AP and 2nd trip echo are clearly visible in the scans and were efficiently removed in regions adjacent to precipitation signal (Fig. 18c). Spurious echo embedded within the precipitation signal (Fig. 18d) was not easily removed without sacrificing convective precipitation.

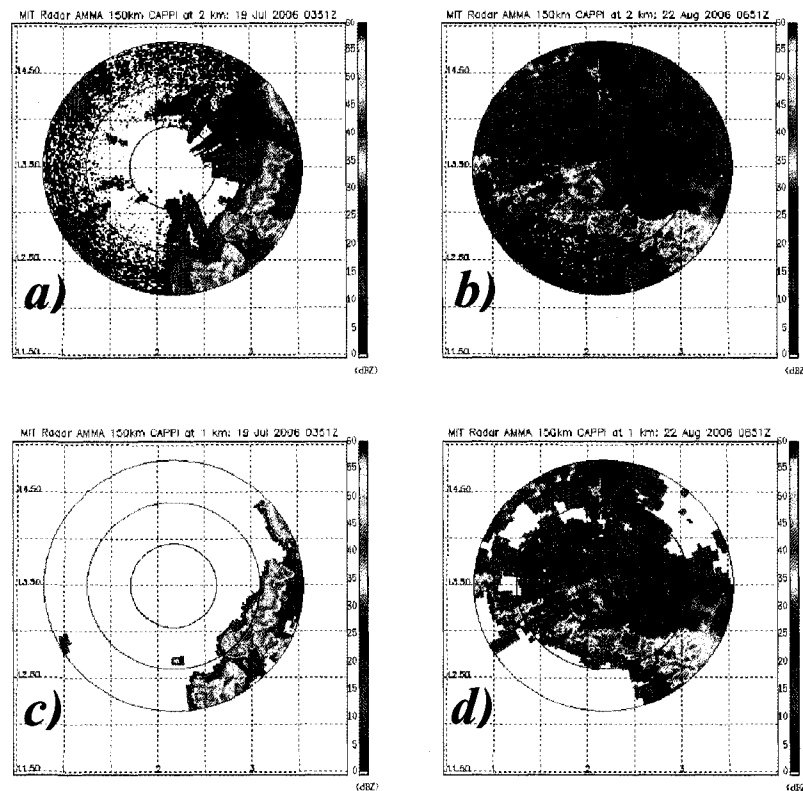


Fig. 18 Examples of before (a-b) and after (c-d) quality control of radar reflectivity scans containing a SLMCS precipitation signal as the system a) enters the scan range and b) passes over the center of the radar scan area by the GVS 1C51 algorithm. Radar range rings are given every 50 km.

As previously explained, the removal of non-meteorological echo resulted in stratiform loss and gaps in MCS stratiform echo (Figs. 19a-d). However, the loss of precipitation due to QC echo removal in the reflectivity range of 1 – 10 dBZ, corresponding to a rainrate range of 0.013 – 0.071 mm·hr⁻¹, is negligible.

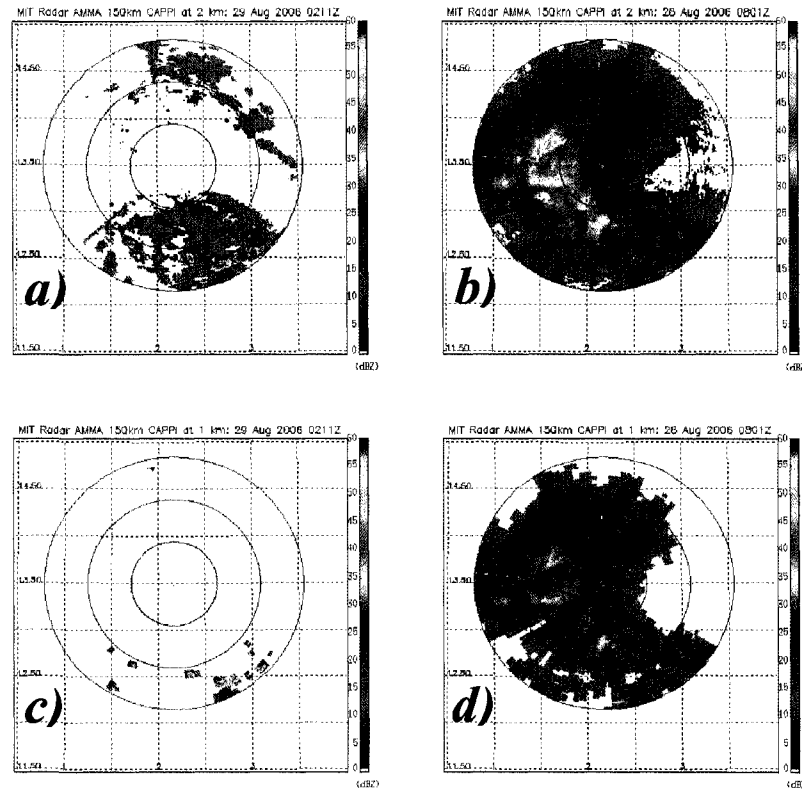


Fig. 19 Examples of before (a-b) and after (c-d) quality control of radar reflectivity scans containing stratiform precipitation signal a) not associated with a large-scale system and b) trailing a SLMCS by the GVS 1C51 algorithm. Radar range rings are given every 50 km.

Per the previous discussion, parameter sets are not only site-dependent, but specific to event occurrence and level of non-meteorological echo within the scan file. A decision tree documenting the appropriate parameter set for various situations is shown in Fig. 20.

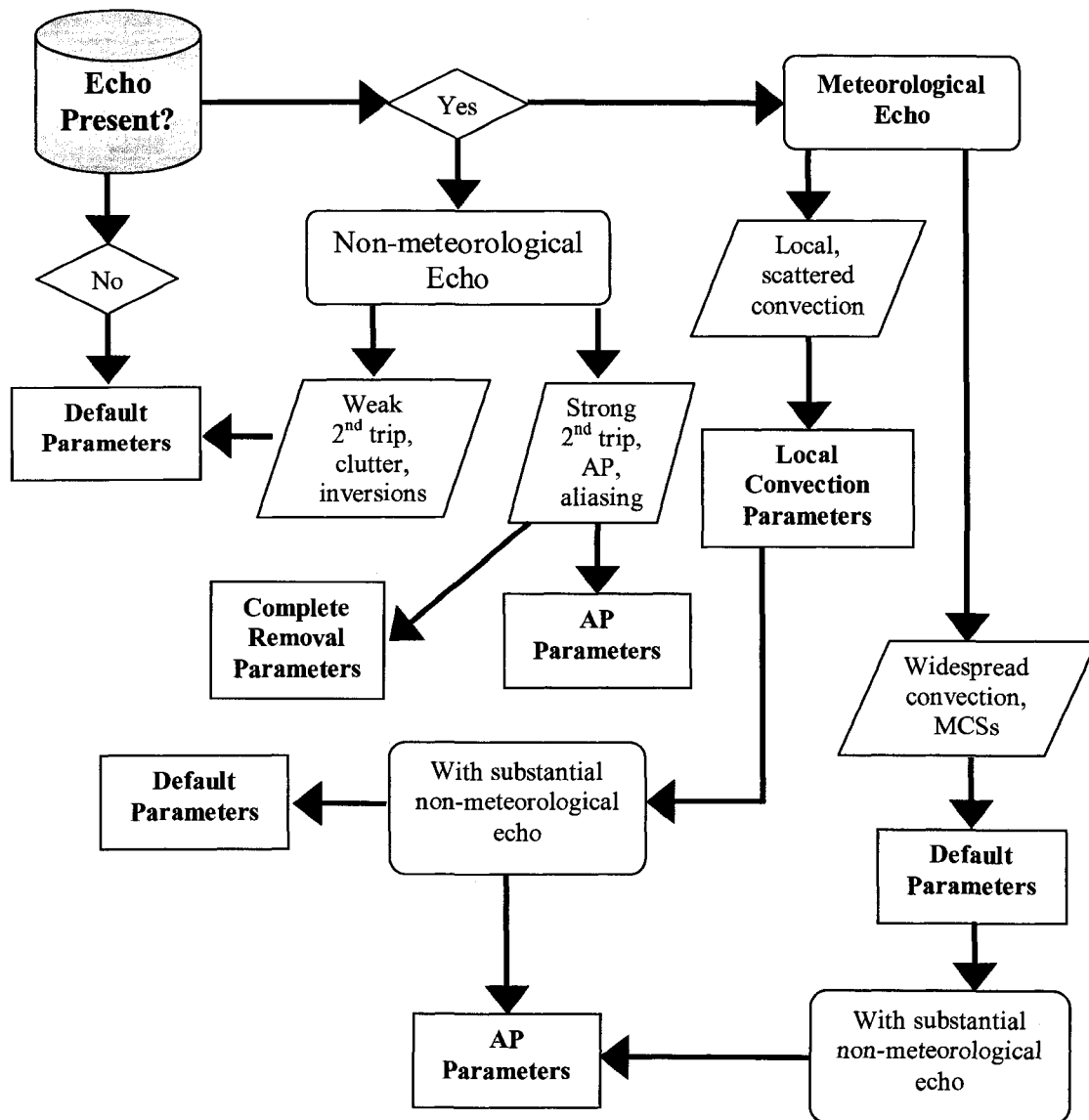


Fig. 20 Flowchart of the decision tree for quality control algorithm application and parameter set used for various radar scan situations.

Analysis of QCed data with respect to raw data was performed to gauge the degree to which the QC algorithm was successful. The QCed dataset was divided by the raw dataset to yield a bias. Rainfall and total area coverage fields were examined for this thesis. The QCed dataset should result in less overall precipitation and areal coverage

than the raw dataset that contained greater amounts of reflectivity. The entire dataset was analyzed and produced similar results.

A bias was calculated by comparing rainrates attained after QC with those before QC (bias = QC / Raw data); values of bias for mean monthly and seasonal rainfall are shown (Table 7). Looking at the month of August, the bias of the means is ~51% for all events, while QCed MCS scale events (not shown) exhibit a bias of means of ~74%. Temporal distribution of bias roughly follows the time series of rainrate values extrapolated from reflectivity data.

Table 7. Mean monthly rainfall and total area per month and seasonally bias calculations during the 2006 West African monsoon season.

	July	August	September	Seasonal Mean
Rainfall Bias	0.3837	0.5061	0.3287	0.4062
Total Area Bias	0.2041	0.3189	0.1725	0.2318

Also shown in Table 7 are monthly and seasonal biases of mean area, where August has a bias of ~32% for all events, while QCed MCS scale events exhibit bias of ~54% of raw data values. The bias distribution follows the monthly rainfall and area coverage discussed later. A lower retention of area coverage is expected, as optimization of the QC algorithm required the loss of stratiform. While the stratiform component contributes a large total amount of echo area, the convective component is more intense and contributes greatly to rainfall totals.

To confirm that the QC algorithm was successful, analysis of the frequency of occurrence of bias fractions was plotted for sub-MCS and MCS-scale events. Bias of

remaining rainfall in MCS-scale events after QC showed a bimodal structure (Figs. 21a-c), with a peak at 0 and ~80% for July, August, and September. September presents a lower frequency due to the fact that less MCS-scale events occurred, resulting in a lower number of files for examination when compared to July and August. Sub-MCS event plots (Figs. 21d-f) are less dramatic for the same reason stated for September MCS cases, though the rough bimodal structure is still visible. The peak at 0% can be explained by the large number of cases in which no precipitation was present in the scan region, so all non-meteorological echo was removed via a complete removal parameter set. The second peak occurring near 80% suggests that in a large number of MCS-scale cases the majority of precipitation was retained. With the frequency between these two peaks low, MCS information retention was achieved.

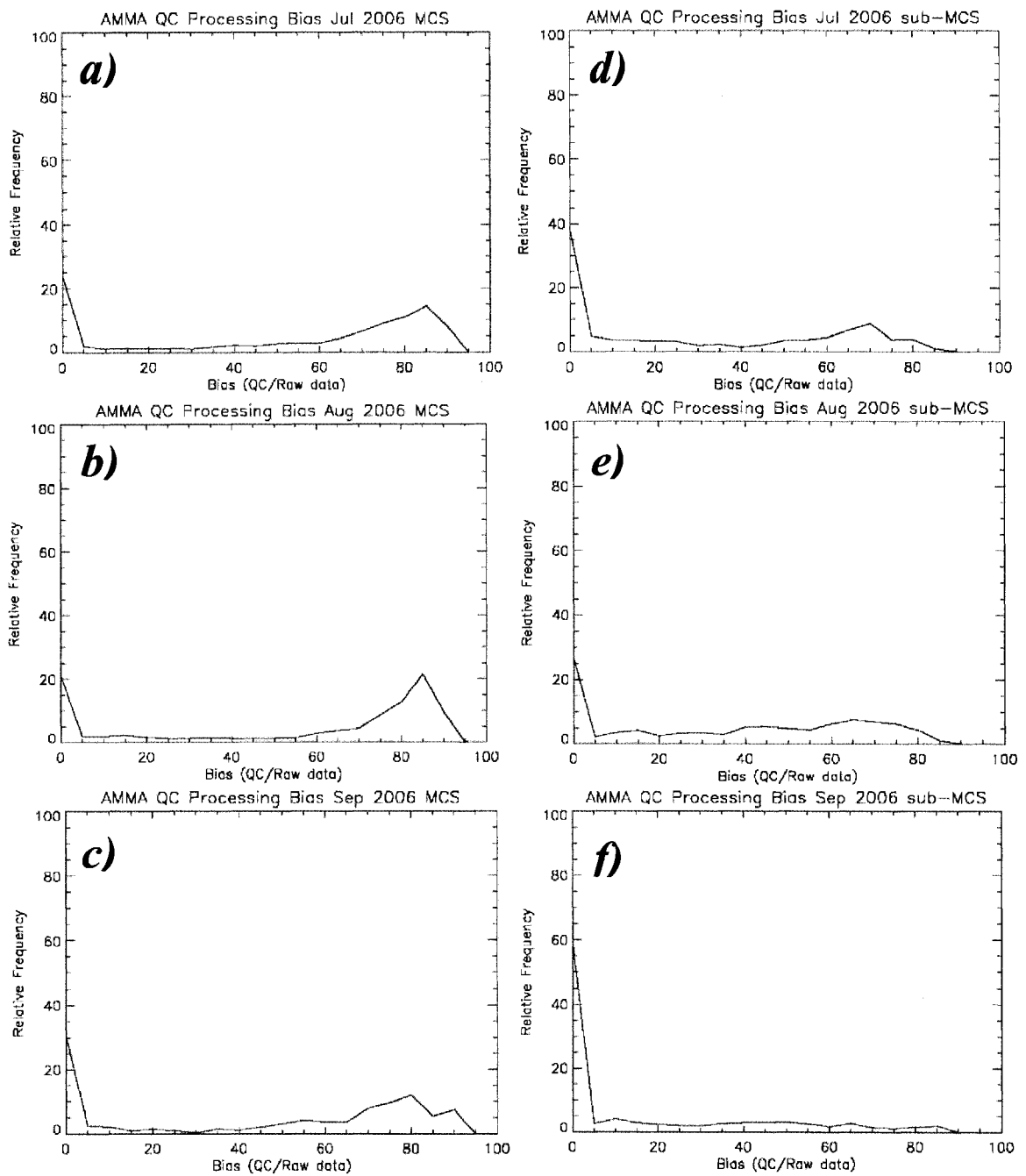


Fig. 21 Relative frequency of rainfall bias (in percent) for July a) MCS and d) sub-MCS scale events; August b) MCS and e) sub-MCS scale events; and September c) MCS and f) sub-MCS scale events.

As suggested by the mean values above, retention of area coverage was not as successful as rainfall. Sacrifice of the stratiform component resulted in much less area associated with the MCS after QC. Frequency distribution of MCS-scale events was broader without substantial peaks outside of the zero peak discussed above (Figs. 22a-c). As mentioned previously, sub-MCS events do not have a large stratiform component and were often accompanied by weak non-meteorological echo. This combination resulted in an apparent low frequency in greater retention of echo area (Figs. 22d-e), though this means that there was a large amount of spurious weak echo that the QC algorithm successfully removed.

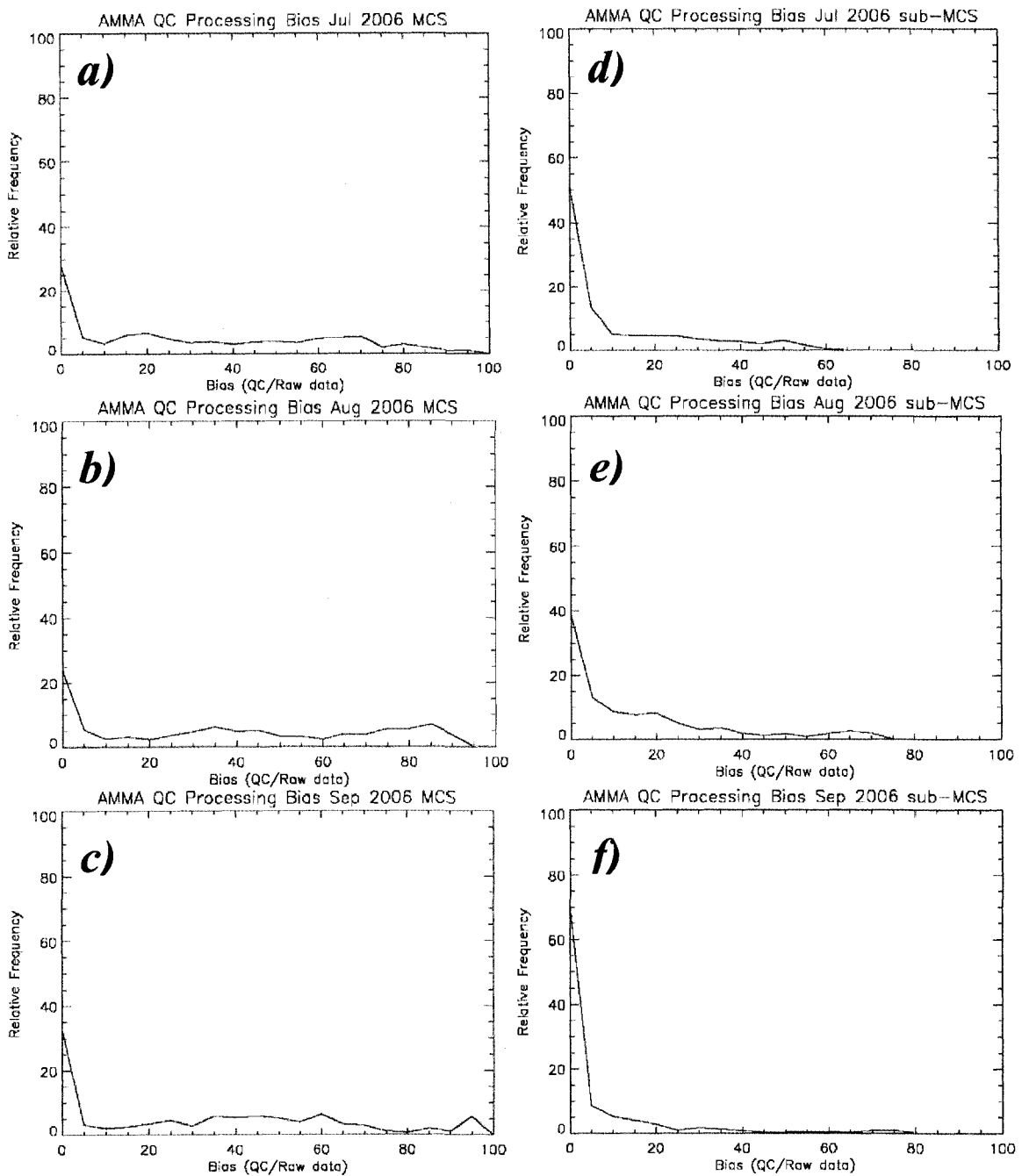


Fig. 22 Relative frequency of total echo cover bias (in percent) for July a) MCS and d) sub-MCS scale events; August b) MCS and e) sub-MCS scale events; and September c) MCS and f) sub-MCS scale events.

b. Rainfall estimates

Rainfall production is forced by the annual variability of moisture fields transported by an advancing ITCZ; on average the ITCZ reaching the most northerly extent in August. Individual storm propagation, duration and occurrence time was of interest for precipitation morphology and structure and characterization of the role of SLMCSs in synoptic-scale patterns.

Le Barbé and Lebel (1997) and Laurent *et al.* (1998) found that July and August represent the “core” of the rainy season, when the greatest frequency of rainfall events occurs. There was an increase leading up to this point with a sharp decrease through October, observed in multiyear rain gauge data. Monthly rainfall rate time series plotted to examine the intensity and variability of precipitation during the monsoon season are shown in Figs. 23-25 for July, August, and September. Unconditional rainrate is defined as the rainrate over the scan region.

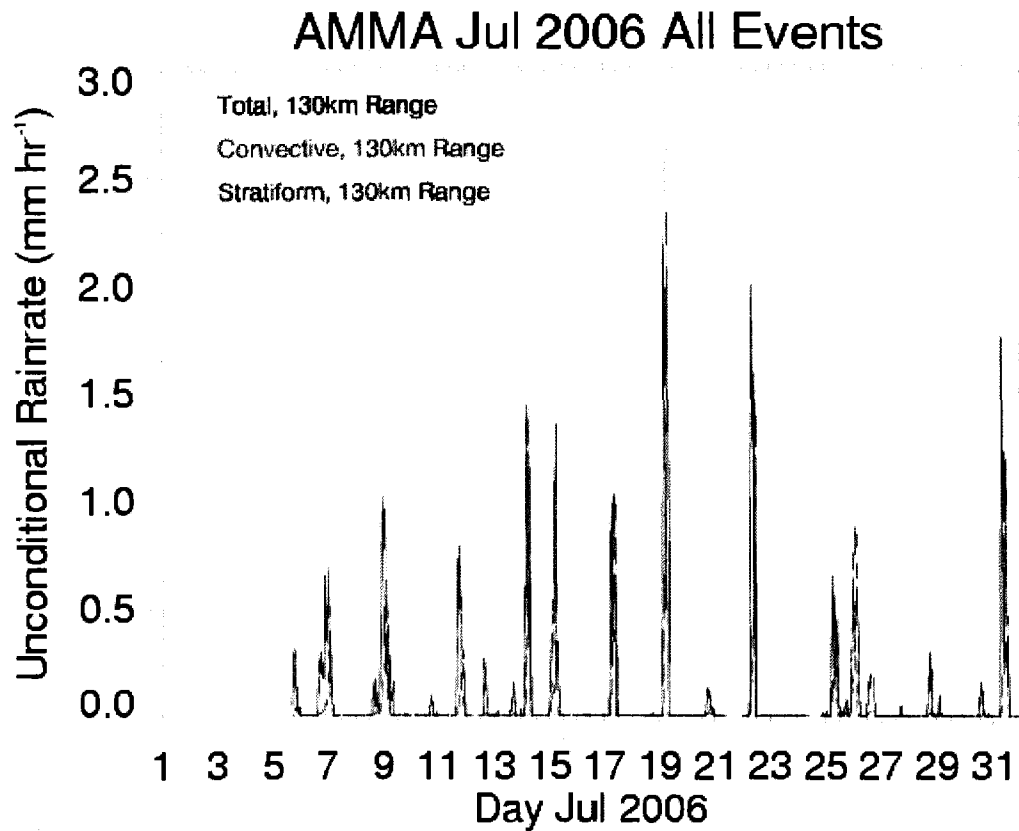


Fig. 23 July radar reflectivity-estimated rainfall rate for total (black), convective (red) and stratiform (blue) precipitation components. This 10 minute interval data indicates the temporal passage of rain events, most with close connection to MCSs.

AMMA Aug 2006 All Events

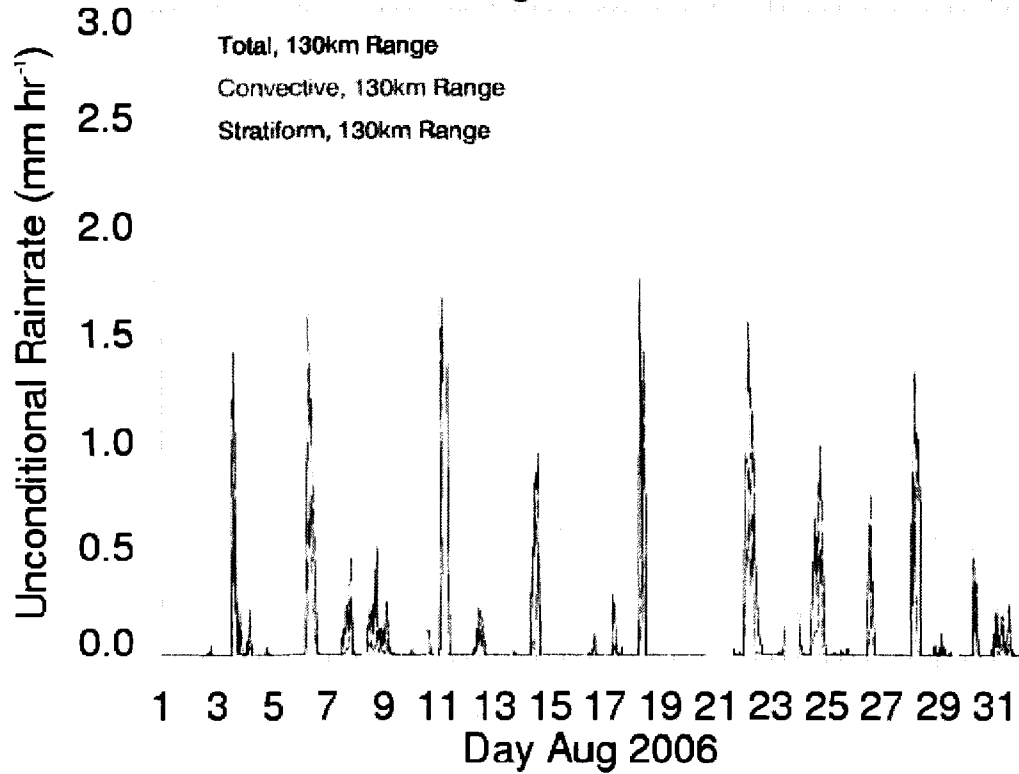


Fig. 24 August radar reflectivity-estimated rainfall rate for total (black), convective (red) and stratiform (blue) precipitation components. This 10 minute interval data indicates the temporal passage of rain events, most with close connection to mesoscale MCSs.

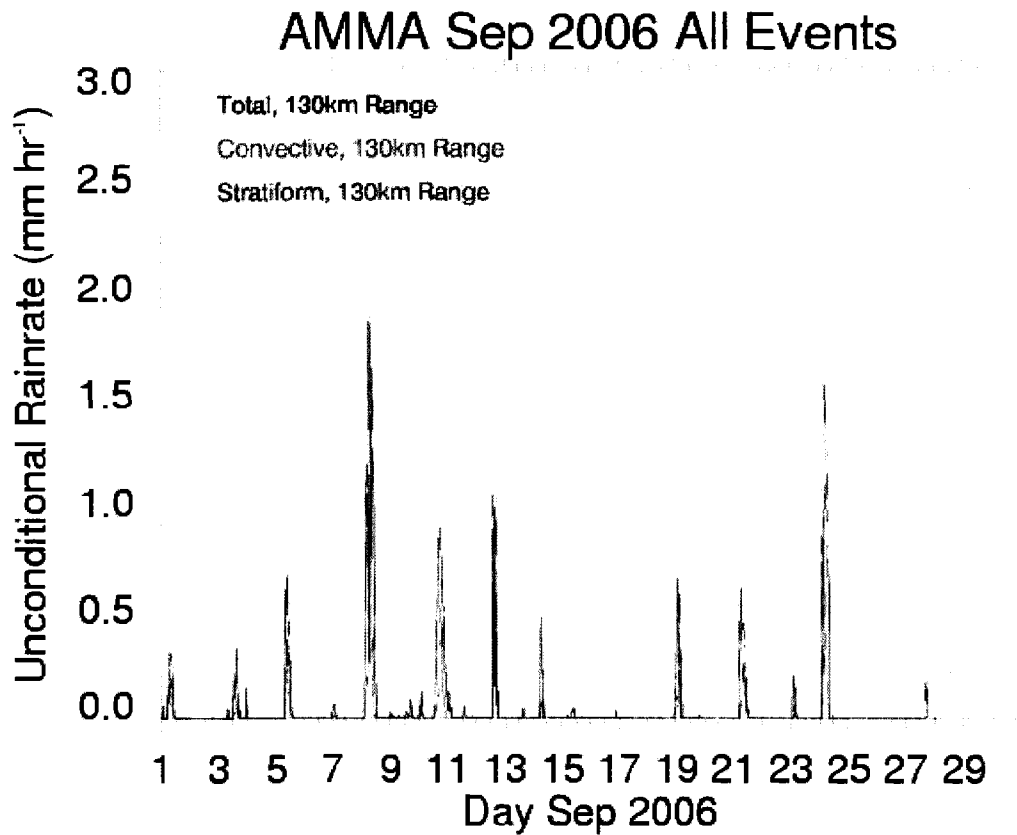


Fig. 25 September radar reflectivity-estimated rainfall rate for total (black), convective (red) and stratiform (blue) precipitation components. This 10 minute interval data indicates the temporal passage of rain events, most with close connection to MCSs.

Though full volume scans were only available starting from 5 July, surveillance scans acquired beginning 24 June, suggested that the monsoon season onset occurred in early July. Local rainfall rate maxima indicate propagation of events across the scan region, where all maxima with peak $> 0.5 \text{ mm}\cdot\text{hr}^{-1}$ were MCS-scale events, with general westward movement. The onset was characterized by active rain events with a maximum rainfall rate $> 2.5 \text{ mm}\cdot\text{hr}^{-1}$, where approximately 25% achieved a rainfall rate $> \sim 1.5 \text{ mm}\cdot\text{hr}^{-1}$. As the monsoon season progressed into August, more frequent and homogeneous rainfall rate events occurred with approximately 40% of the events near $1.5 \text{ mm}\cdot\text{hr}^{-1}$. The end of the monsoon season in September recorded less frequent and less active storms, where only $\sim 17\%$ possessed a rainfall rate of $\sim 1.5 \text{ mm}\cdot\text{hr}^{-1}$.

MCS-scale storm duration displayed large variability throughout the monsoon season (Fig. 26), where storm duration was defined as the time from when a MCS propagated into the radar scan region until trailing stratiform precipitation associated with the system dissipated or departed the sample area. SLMCS sampling times ranged from ~ 2 -28 h, with a mean of 12.1 h, with mean monthly event duration decreasing throughout the season.

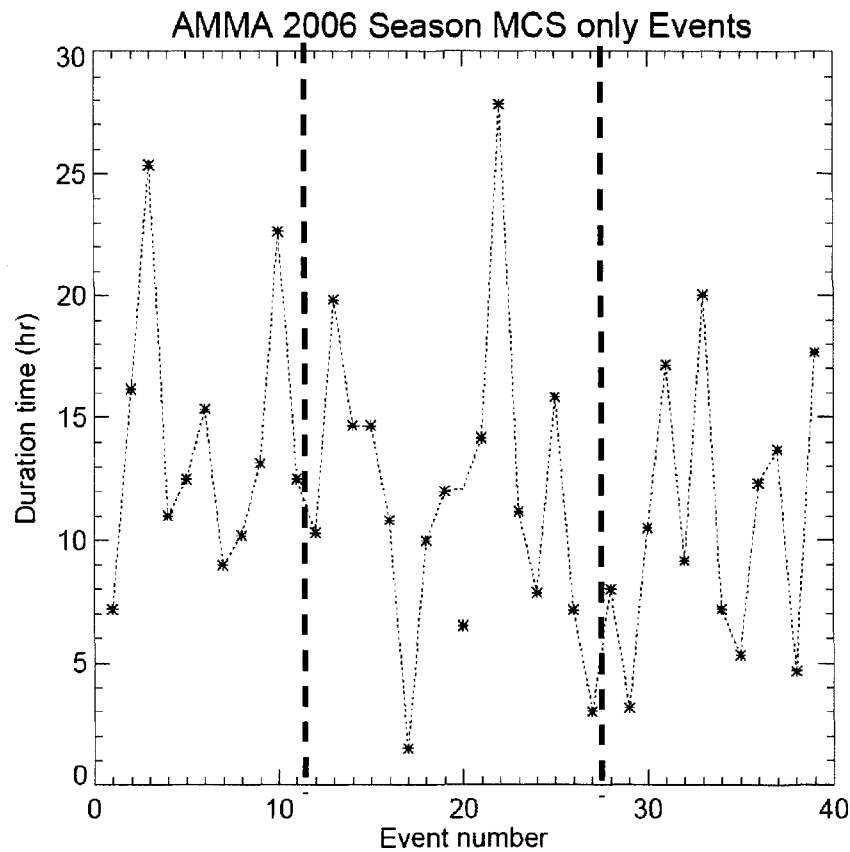


Fig. 26 Duration of MCSs throughout the West African monsoon season. Regions are divided (heavy vertical dashed line) based on month in which system occurred.

Previous studies report SLMCS lifetimes between 10-13 h (Aspliden *et al.* 1976; Payne and McGarry, 1977; Rowell and Milford, 1993; Fink and Reiner 1999). Results from this study likely underestimate actual storm duration, because stationary, ground-based radar limits the observation field and may not record the full lifetime of a storm. The decreasing duration could suggest SLMCSs occur with greater speed at the beginning of the season; however, if genesis location was temporally dependent, there is no way to verify this with radar data alone. However, event duration revealed the time interval that

each MCS impacted the local region; an important parameter in whether or not this was controlled by system lifetime or system propagation.

Relation of precipitation events to prevailing larger scale flow was analyzed via spectral analyses of rainfall time series. The Fourier transform technique was applied, in which the rainfall time series were decomposed into sinusoidal components. Specifically a fast Fourier transform (FFT) algorithm, which allows more efficient processing of the discrete Fourier transform as fewer computations are required, was applied. The FFT reveals periodicities in a data set and the relative strength of the periodic components.

Data series were divided in two distinct sets for analysis; separated by month and also bisected into approximately equal time periods. Both data groups yielded similar results, suggesting a robust confirmation of storm frequency. A strong one day diurnal harmonic was found, as expected, and a 2-4 d frequency of SLMCS event passage (Fig. 27) was extrapolated. The latter suggests a direct connection to AEWs and will be expanded upon in section 4f. FFTs of monthly rainfall data, shown in Fig. 27, are noisy as a result of the chaotic nature of rainfall. Application of low-, high- and band-pass filters resulted in the loss of significant rainfall event period information, suggesting that both high and low frequency forcing are key contributors to the variability of WAM precipitation.

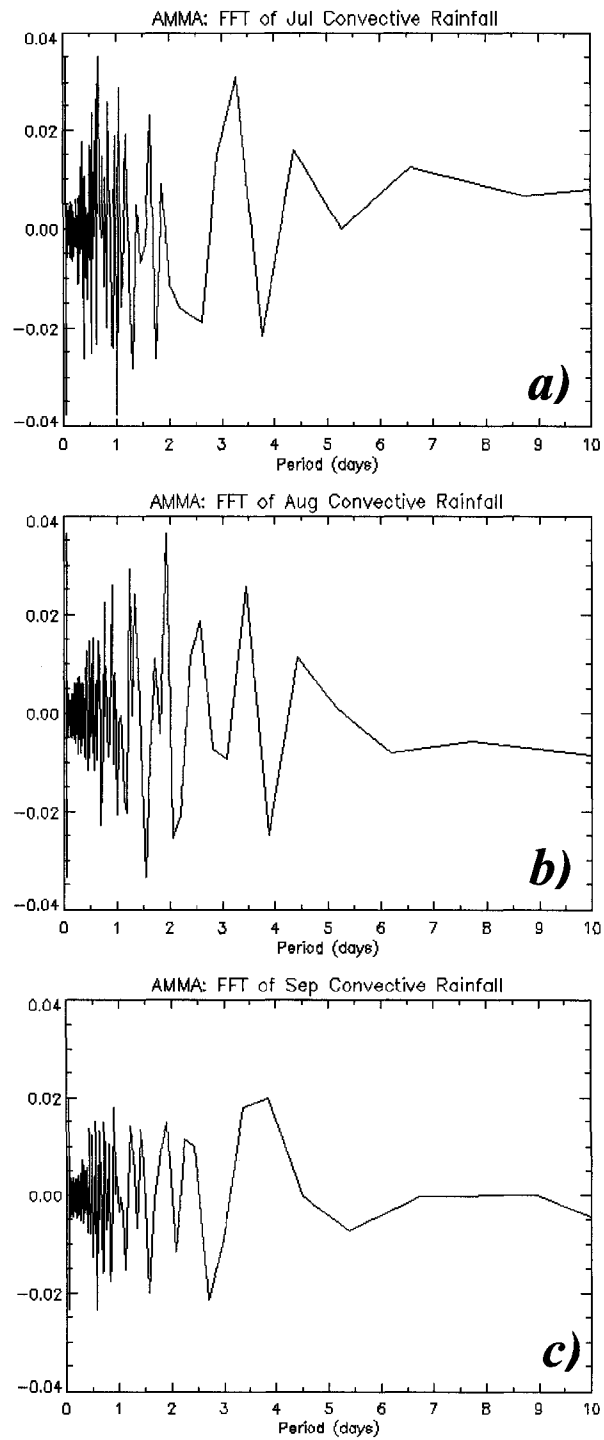


Fig. 27 Spectral analyses of monthly rainfall time series data to assess periodicity of dataset. Fourier transform algorithm analysis of rainfall frequency is shown for a) July, b) August, and c) September.

c. Rainfall and area coverage

MCS events dominated (88%) the total precipitation during the wet season and contained a larger convective rain fraction at the start of the season compared to later months (Fig. 28), with a decrease in each subsequent month. Laurent *et al.* (1998) found a similar fraction of MCS precipitation (of total) at 95% with the EPSAT - Niger rain gauge dataset. As expected, convective rain contributed the majority of total rainfall during the WAM season (59%), with July possessing substantially higher convective rain fraction than August and September.

AMMA 2006 MCS Rainfall

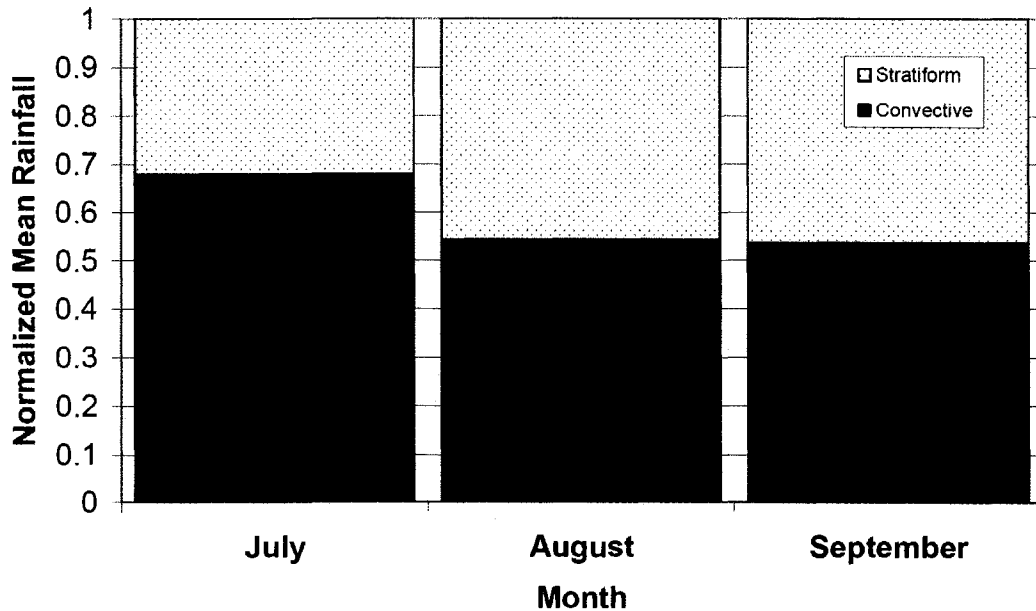


Fig. 28 Monthly convective (dark) and stratiform (light) rainfall portions of total precipitation in MCSs, in terms of radar reflectivity-converted rainrate per hour.

Conditional rainfall rates, defined as rainrate in area where rain occurs, revealed that July experienced the highest fraction of convective precipitation. By definition

conditional rainrates may be viewed as rainrate per unit area, or intensity of rainfall. This suggests that July events were the most intense of the season. July also possessed the highest convective rain fraction for sub-MCS scale systems, suggesting greater local instability near the beginning of the season, preceding synoptic-dominated forcing found as the season progressed. Larger convective rain fractions are consistent with weaker synoptic forcing (leading to less synoptic-scale weak ascent and thus less stratiform rain), lifting and moistening in easterly wave troughs, earlier in the season as discussed later.

As expected for the Sahel region, observed monsoon MCSs exhibited the trailing stratiform structure discussed earlier, resulting in mostly stratiform (87%) mean SLMCS precipitation area. Using a slightly different definition discussed earlier, Mathon *et al.* (2002) found that 78% of cloud cover was associated with OCSs, a sub-group of MCSs, while this study finds that 85% of echo area results from MCSs. The monsoon season peaked in intensity in terms of precipitation and number of events in August. This would suggest that synoptic forcing was greatest at this time due to greater easterly wave activity as the ITCZ reaches the furthest north before receding back toward the equator. This forcing leads to the largest SLMCS area in August at ~6 % of total scan area, while July SLMCSs cover ~4 % of the total area and September ~3 % of scan area. Because the WAM is defined in terms of rainfall this suggests the season peaks in August along with the largest number of systems and area covered. Figure 29 shows area coverage normalized to the total area covered each month, suggesting that July convection represents a larger portion of area coverage of SLMCS storms. The vertical axis in Fig. 29 has an upper limit of 0.2 to display characteristics of the convective portion. Due to

the fact that the convective component is a small portion of the total area coverage, the display has been modified to highlight the most interesting features. Stratiform coverage encompasses the remainder of the normalized mean area to unity.

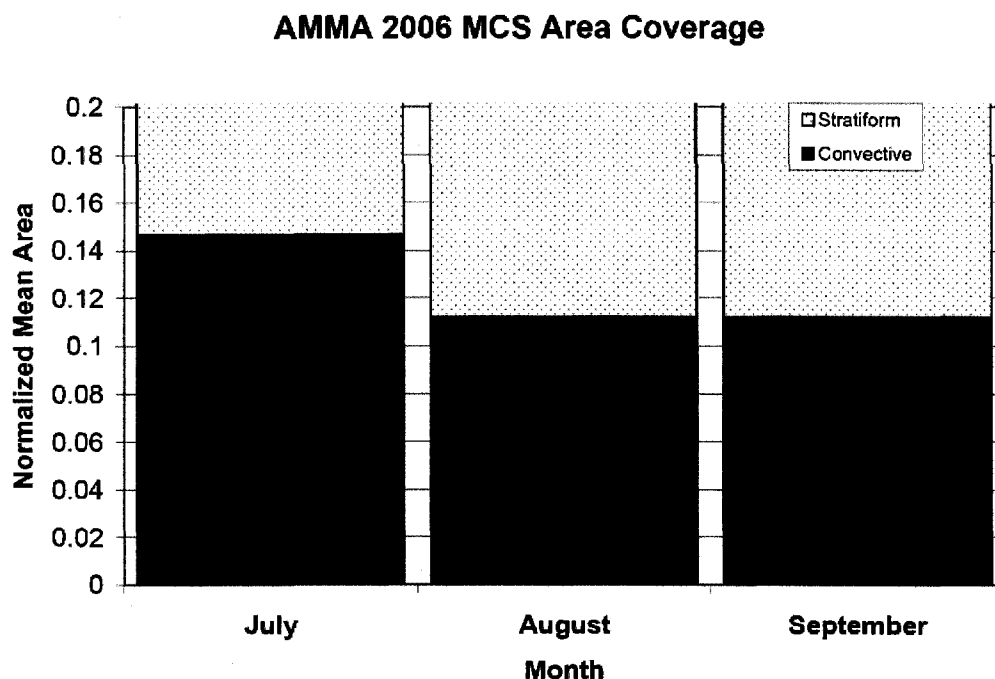


Fig. 29 Monthly convective (dark) and stratiform (light) portions of total areal coverage encompassed by MCSs. Each month is normalized separately against total area covered by MCSs.

d. Diurnal composites

Monthly diurnal composites were constructed separately for SLMCS (Fig. 30) and sub-MCS scale events (Fig. 31). The vertical scale of Fig. 30 is approximately ten times greater than that of Fig. 31, showing that MCS systems provided a much larger contribution to rainfall than sub-MCS systems. The peak in the SLMCS diurnal composite plot showed a strong preference to pass through the radar domain near sunrise (07 UTC), occurring every 2-4 days according to spectral analysis and observations. A

late afternoon peak in the sub-MCS diurnal composite can be related to afternoon convection resulting from surface heating throughout the day.

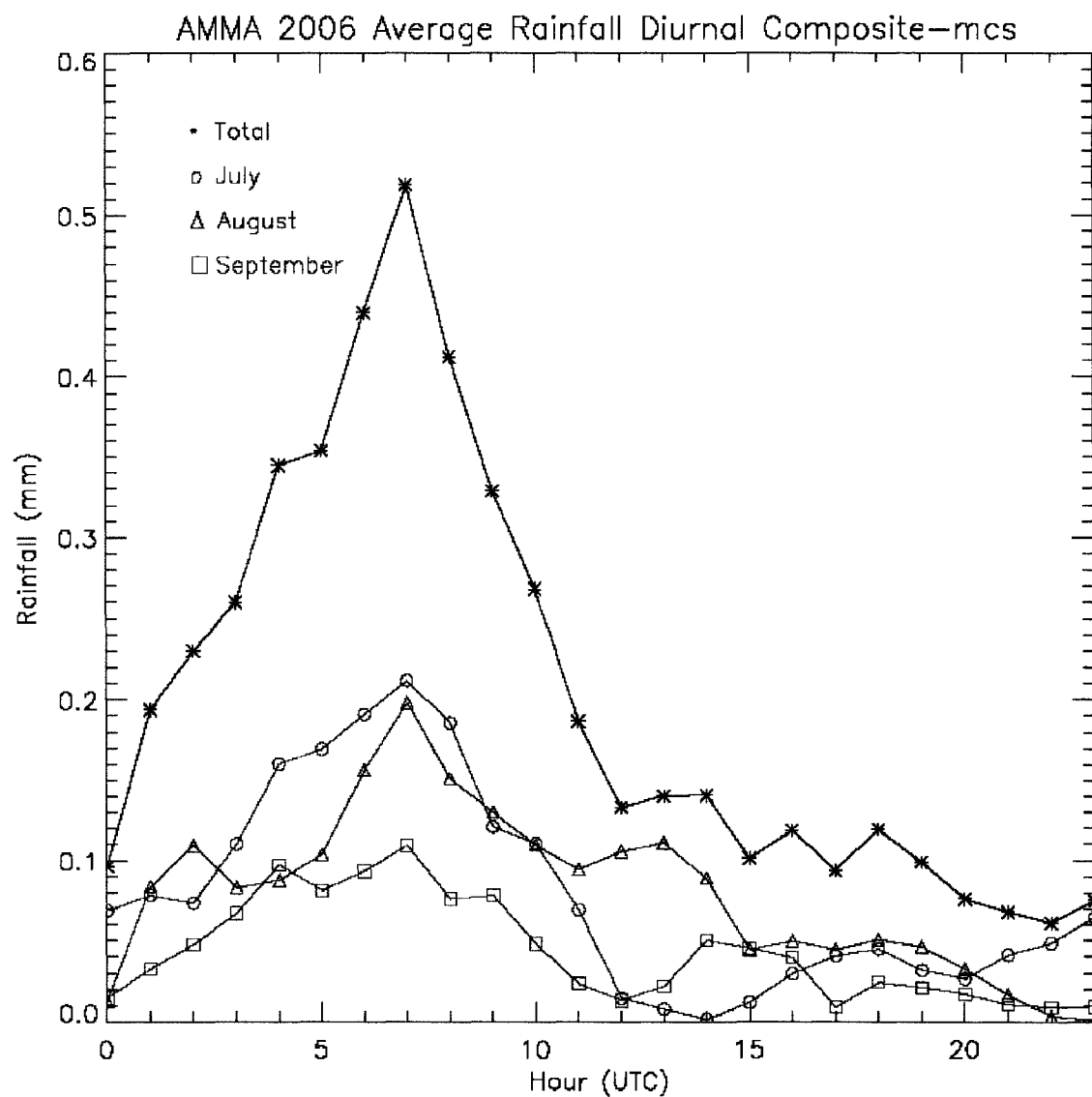


Fig. 30 Seasonal diurnal composite of average rainfall for SLMCSs. Seasonal total (black) of July (red), August (blue), and September (green) are plotted as a function of hour of day.

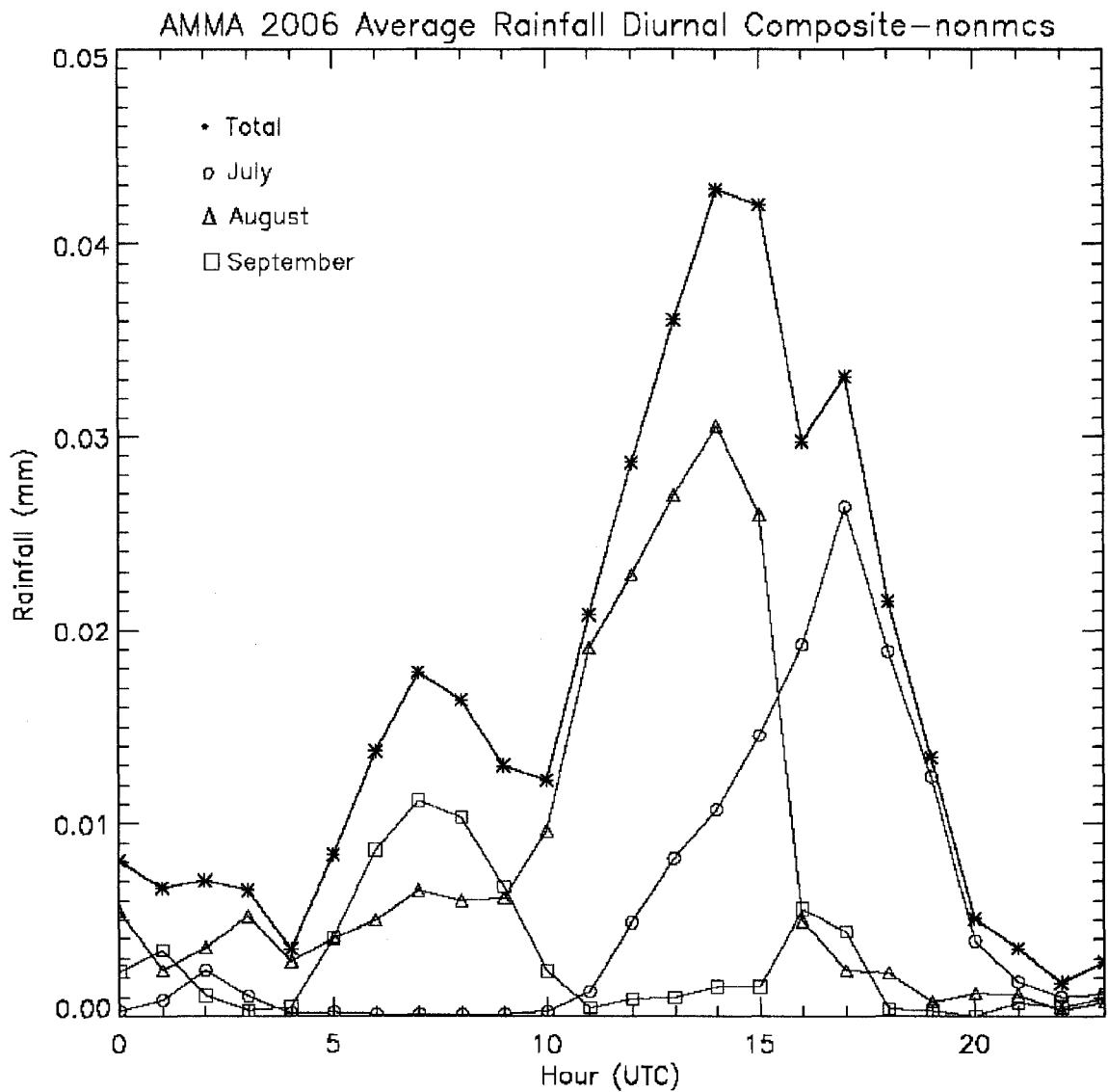


Fig. 31 Seasonal diurnal composite of average rainfall for sub-MCS events. Seasonal total (black) of July (red), August (blue), and September (green) are plotted as a function of hour of day.

A frequency distribution of SLMCS passage during the WAM season is shown in Fig. 32, where passage is defined as the time when the storm was located over the center of the radar scan area. A clear preference for morning hours is observed with a peak at 07 UTC, with a small secondary peak of only three occurrences centered near 14 UTC. This diurnal phase-locking suggests a common temporal and spatial SLMCS origin east of Niamey, with system generation linked to AEW propagation. The small secondary peaks seen in the afternoon suggest an alternative genesis connected to local convective forcing (diurnal cycle).

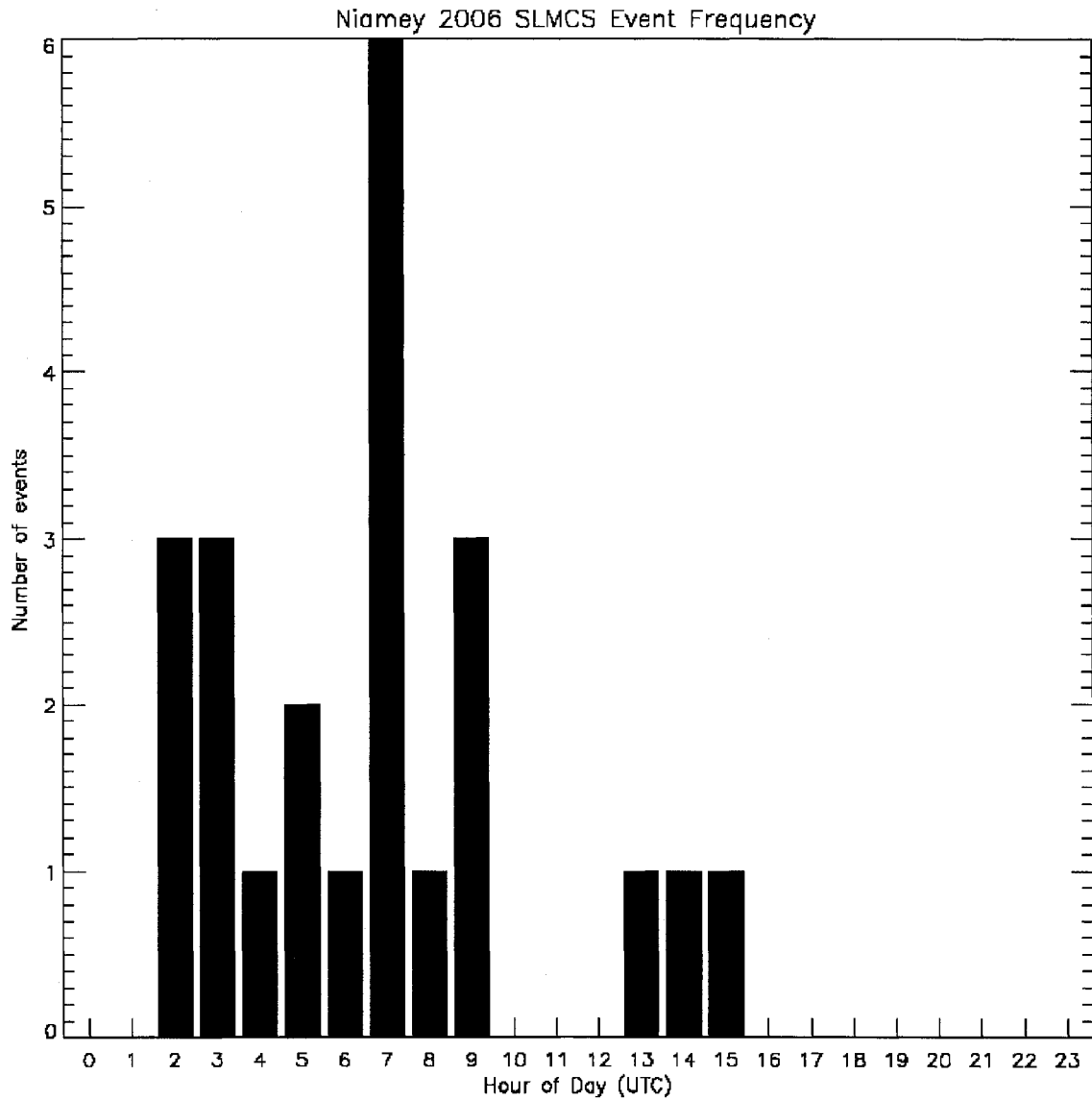


Fig. 32 Frequency histogram of SLMCS passage over radar during the West African monsoon season in Niamey, Niger.

Examination of diurnal data from the EPSAT - Niger experiment by Shinoda *et al.* (1999) shows a strong precipitation signal at 08 UTC, which compares well with the results from this study. Mathon *et al.* (2002) confirm the idea posited by Shinoda *et al.* (1999) that the early morning Niamey precipitation signal is resultant from SLMCS

genesis at a point east of the radar area, by plotting system genesis location. Generation often occurs in the afternoon over eastern Niger at the southern end of the Air Mountains, and propagation speeds place them in the Niamey area during nocturnal hours. Ferreira *et al.* (2008) provide a similar conclusion for the radar dataset used in this study through satellite analysis of SLMCS and easterly wave genesis.

Slight difference in precipitation maxima could result from the difference in analysis technique from study to study. For example, a three hour average of rainfall data was used by Shinoda *et al.* (1999), while this study worked with one hour averages. Variable average AEW propagation speeds (Fink and Reiner 2003; Berry *et al.* 2007) may transport disturbances at different rates through sample regions, while SLMCSs embedded near troughs would experience a range of propagation speeds (Aspliden *et al.*, 1976; Fink and Reiner 1999). Mathon *et al.* (2002) also confirm a nocturnal precipitation signal.

Sub-MCS events (Fig. 33) were locally generated in the late afternoon, with a seasonal average of 15 UTC, by solar heating resulting in small-scale instability. Monthly data shows some variability, with an August maximum occurrence 2-3 hours earlier. Figure 33 shows scattered, isolated convection to the west and south of the radar. This represents a typical local convection scenario, with generally smaller events, but ranging in size and localization. Reflectivity shows that these events are primarily associated with a small convective core without a great deal of stratiform surrounding the core.

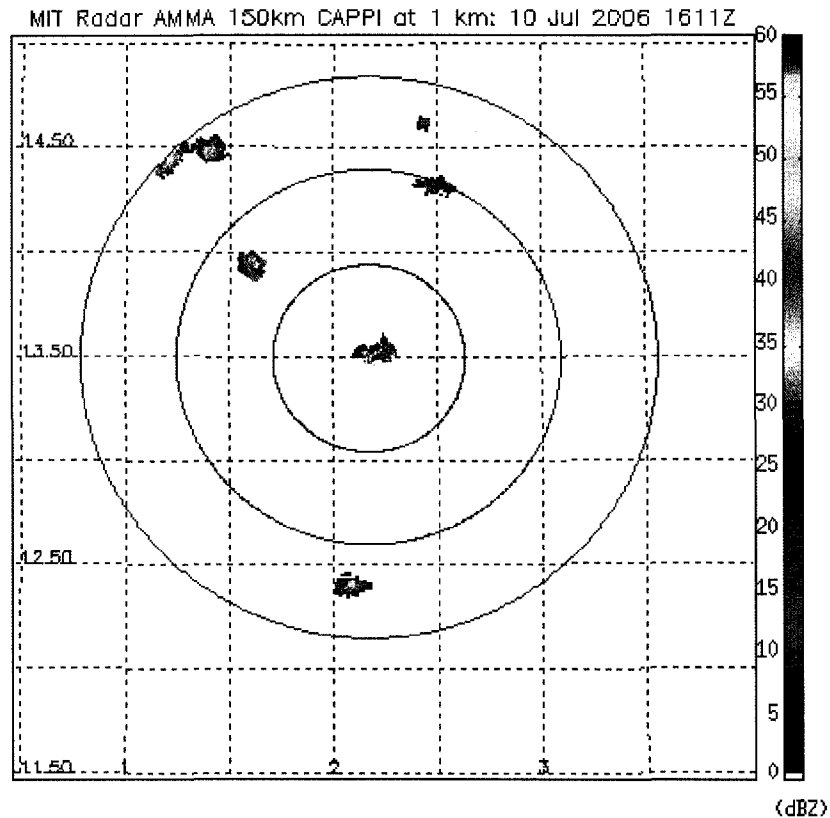


Fig. 33 Isolated local convection in south and western portion of the radar scan domain during the afternoon of 10 July 2006. Radar range rings are given every 50 km.

Shinoda *et al.* (1999) show the same temporal relationship of convective occurrence, though seasonal data is used and therefore finer-scale time resolution is not possible. This study hypothesizes that stronger synoptic forcing in mid-season likely weakened convective inhibition (CIN), resulting in rain initiation earlier in the day during August compared to other months. Convective available potential energy (CAPE) is highly dependent upon air mass properties. The furthest northward progression of the ITCZ occurs during August, bringing more moisture and higher relative humidity values, which in turn increase CAPE. Figure 34 shows 10 day rainfall estimates for a) January (winter),

b) April (spring), c) August (summer), and d) November (fall) based on satellite and rain gauge data generated by the Climate Prediction Center

(<http://www.cpc.ncep.noaa.gov/products/fews/rfe.shtml>).

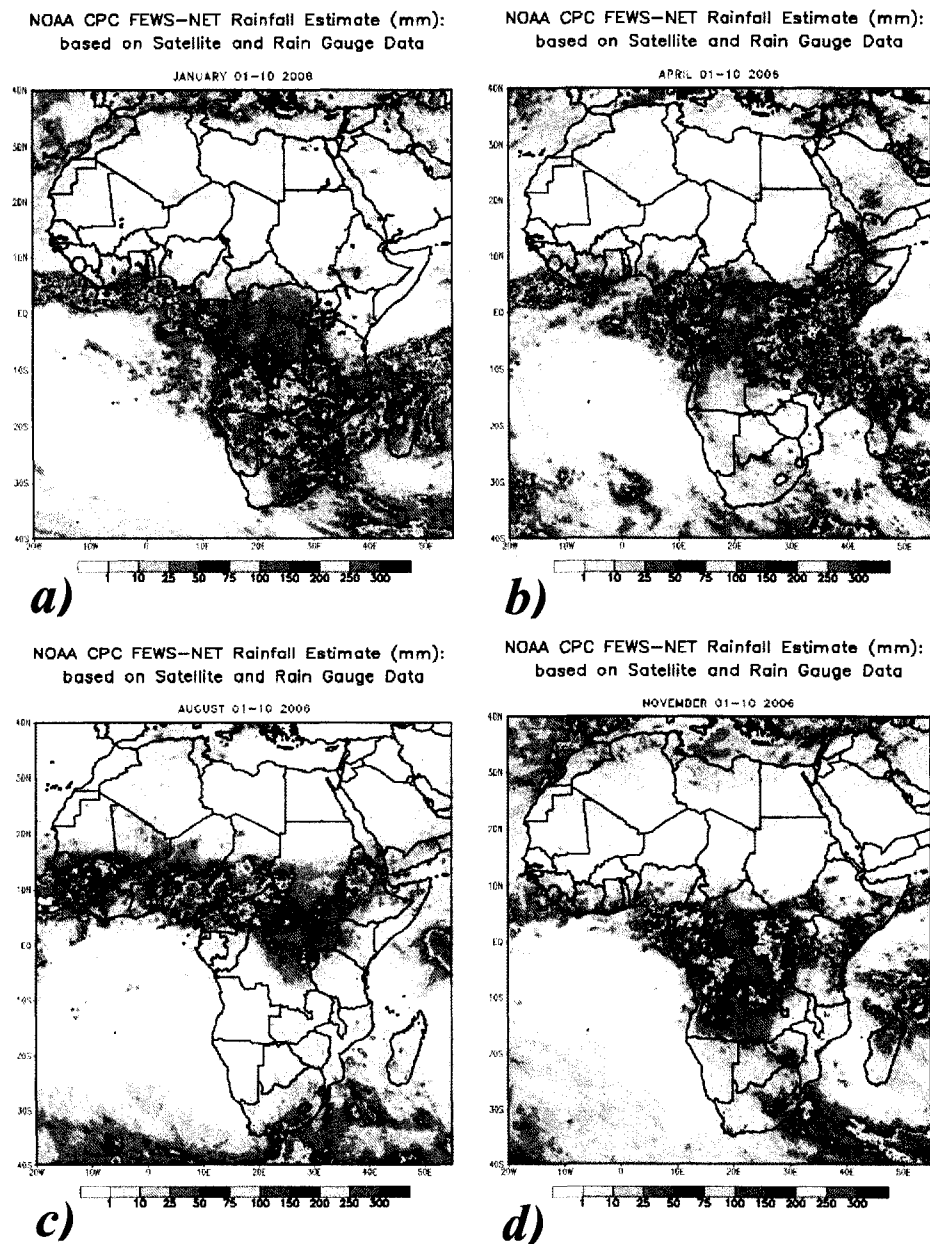


Fig. 34 Rainfall estimates for a) January (winter), b) April (spring), c) August (summer), and d) November (fall) derived from satellite and rain gauge data. Plots generated by the Climate Prediction Center (<http://www.cpc.ncep.noaa.gov/products/fews/rfe.shtml>).

The moist air mass is transported north into eastern Africa and then transported west over Niamey by synoptic flow resulting in convective genesis. Vertical transport of moist air in large-scale ascent from synoptic forcing in the region may have weakened CIN and lowered the threshold of daily heating required for convective initiation (thus earlier diurnal convection).

e. Vertical structure

The WAM supplies a large amount of rainfall to the Niamey region, with contributions from both sub-MCS and MCS-scale systems. Though SLMCSs contribute the vast majority of precipitation, sub-MCS events are also important in understanding the underlying dynamics involved in storm generation and structure for the Niamey region. Large amounts of precipitation are often associated with deep convection. Petersen and Rutledge (2001) note that cloud cover and lightning flash density, both used as indicators of deep, intense convective rainfall, may not present a completely accurate picture of precipitation capability. Demott and Rutledge (1998a) found that over the tropical oceans where warm rain processes are important, the vertical depth of convection does not necessarily correlate with heavy rainfall. Over land, heavy tropical rainfall is better correlated with deeper convection (Zipser 1994).

Mean vertical reflectivity profiles for the 2006 WAM season were created, with analysis limited to below 13 km, where areal coverage of radar echo was at least 15% of coverage at the 1 km analysis height (Yuter and Houze 1995). Profiles were calculated for the entire season and monthly for July, August, and September (Fig. 35). Output was

divided into three panels: all events, convective, and stratiform components (according to the convective-stratiform partitioning discussed in section 3e). Maximum reflectivity values are recorded between 3-4 km AGL, with July exhibiting stronger reflectivity values than August and September. The profiles indicate that July exhibits deeper convection, indicated by higher reflectivity values aloft, implying stronger convective updrafts lifted larger ice particles higher in the storm, enhancing the precipitation process. This strengthens results shown in Figs. 23-25 revealing July to have higher rainrate values than August and September, suggestive of more intense precipitation. Events in July were less numerous than August, however, yielding less total rainfall.

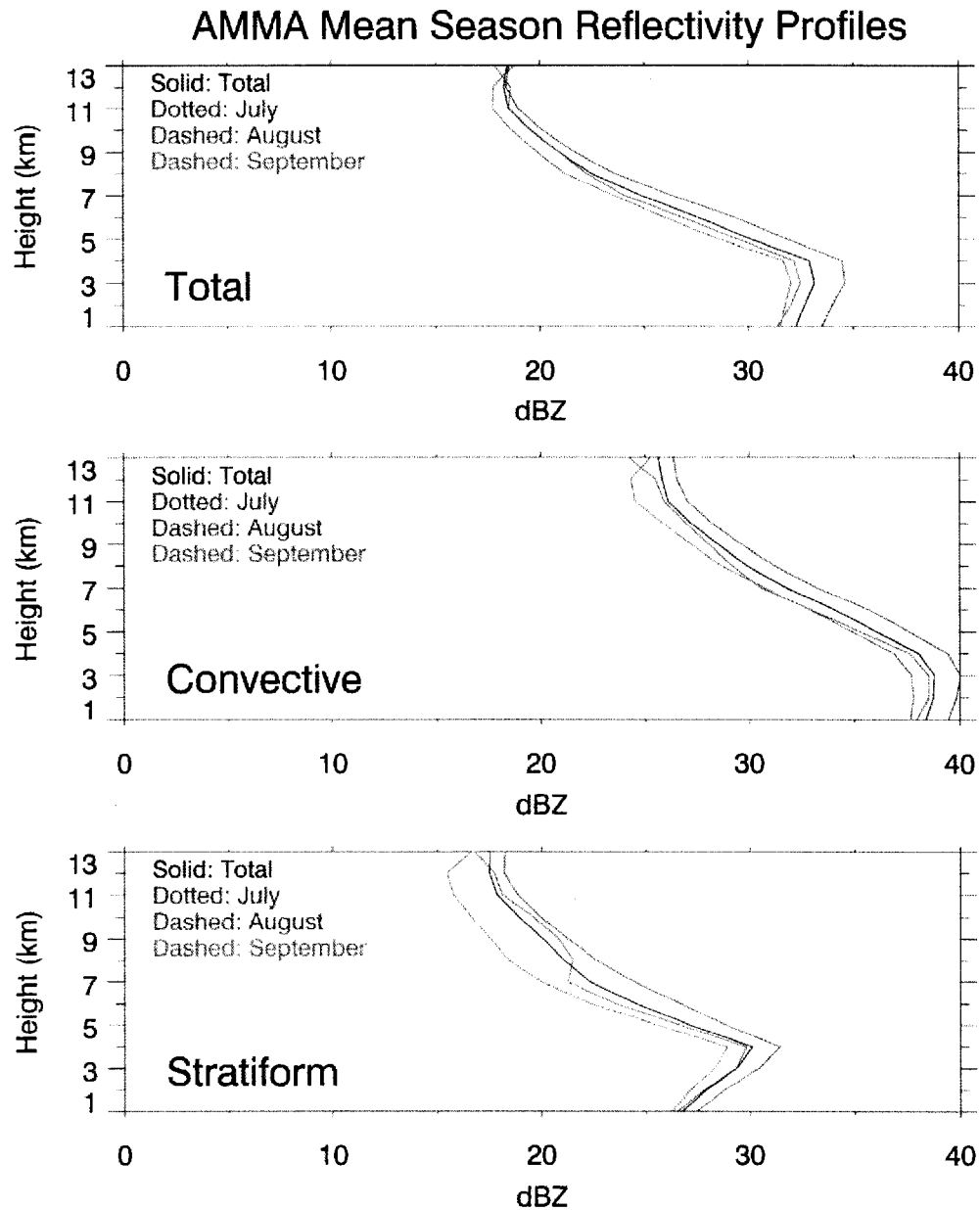


Fig. 35 MIT radar mean vertical reflectivity profile for the 2006 West African monsoon season (black); and sub-divided by month: July (green) and August (red) and September (blue). The top panel represents all events, while the middle and bottom panels show convective and stratiform components of the events, respectively.

Vertical structure of observed SLMCSs were likely similar to tropical continental systems studied previously (Petersen and Rutledge 2001; Rickenbach *et al.* 2002). Then assuming a nominal melting level of 5 km altitude, results summarized by Petersen and Rutledge (2001) indicate that profiles with reflectivities ≥ 30 dBZ concentrated below the freezing level suggest dominant warm rain convective processes. The difference between mean reflectivity values increased more quickly with height in July than the other months up to the freezing level for total, convective, and stratiform areas. Yet, above the nominal melting level, the July profiles were several dB higher than August or September. This suggests increased water mass in the lower and upper troposphere in July when compared to August and September, consistent with both an enhanced warm rain process and stronger updrafts.

Next the seasonal mean vertical reflectivity profile was separated into SLMCS and sub-MCS events, with profiles calculated for both cases (Fig. 36). Comparing the curves reveals that the seasonal profile of all events is most heavily influenced by the SLMCS case, which is likely due to SLMCS events providing the majority of precipitation through the season. The SLMCS mean vertical reflectivity profile is much different than that of sub-MCS events. When comparing the SLMCS case and the sub-MCS cases, the relative reflectivity value maximum for the sub-MCS case occurs slightly lower than the SLMCS case at ~ 3 km, but the reflectivity value does not substantially change throughout the vertical profile. It is apparent that the SLMCS case exhibits higher reflectivity values up to ~ 7 km, at which point the opposite is true. This is suggestive of intense small-scale convection, supporting the notion that strong diurnal

forcing allows for deep vertical development. These storms are small and short-lived, however, producing a small sample size which introduces inherent statistical noise into profile analysis. It is shown that sub-MCS convection does not provide a great deal of rainfall over the course of the WAM season. The fact that SLMCS cases show greater reflectivity values to the mid- to upper-troposphere (7 km) suggests that synoptic forcing associated with SLMCS systems plays a greater role during the monsoon season.

AMMA Mean Season Reflectivity Profiles

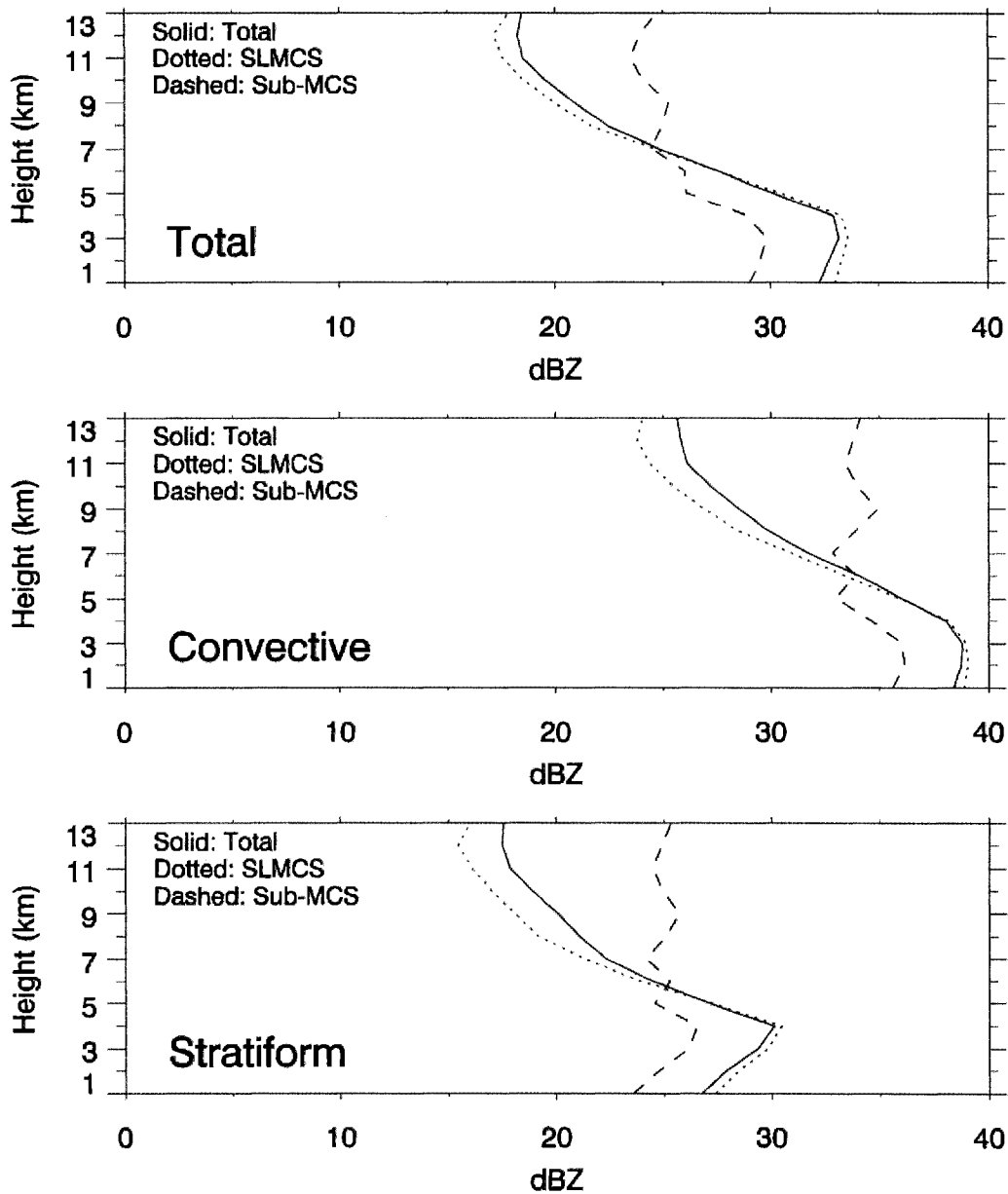


Fig. 36 MIT radar mean vertical reflectivity profile for the 2006 West African monsoon season (solid line); and sub-divided into SLMCS (dotted line) and sub-MCS (dashed line) scale components. The top panel represents all events, while the middle and bottom panels show convective and stratiform components of the events, respectively.

Time series of mean 30 dBZ contour heights were constructed as a measure of convective intensity (Fig. 37). Data were summed into one day intervals for averaging, effectively applying a time filter that reduced the short-term variability of the dataset. The daily rainfall values were normalized to monthly maximum values to provide correlation between contour heights and rainfall. Monthly averages of mean 30 dBZ contour heights were calculated with July at 1.68, August at 1.65, and September at 1.11 km. This suggests that July possessed more intense convection, but due to less frequent events, August produced more monthly rainfall. Fig. 37 suggests an irregular 7-10 day variation in mean convective strength, a timescale greater than the 3-5 day AEW variability. Future work will investigate the synoptic factors controlling changes in vertical structure.

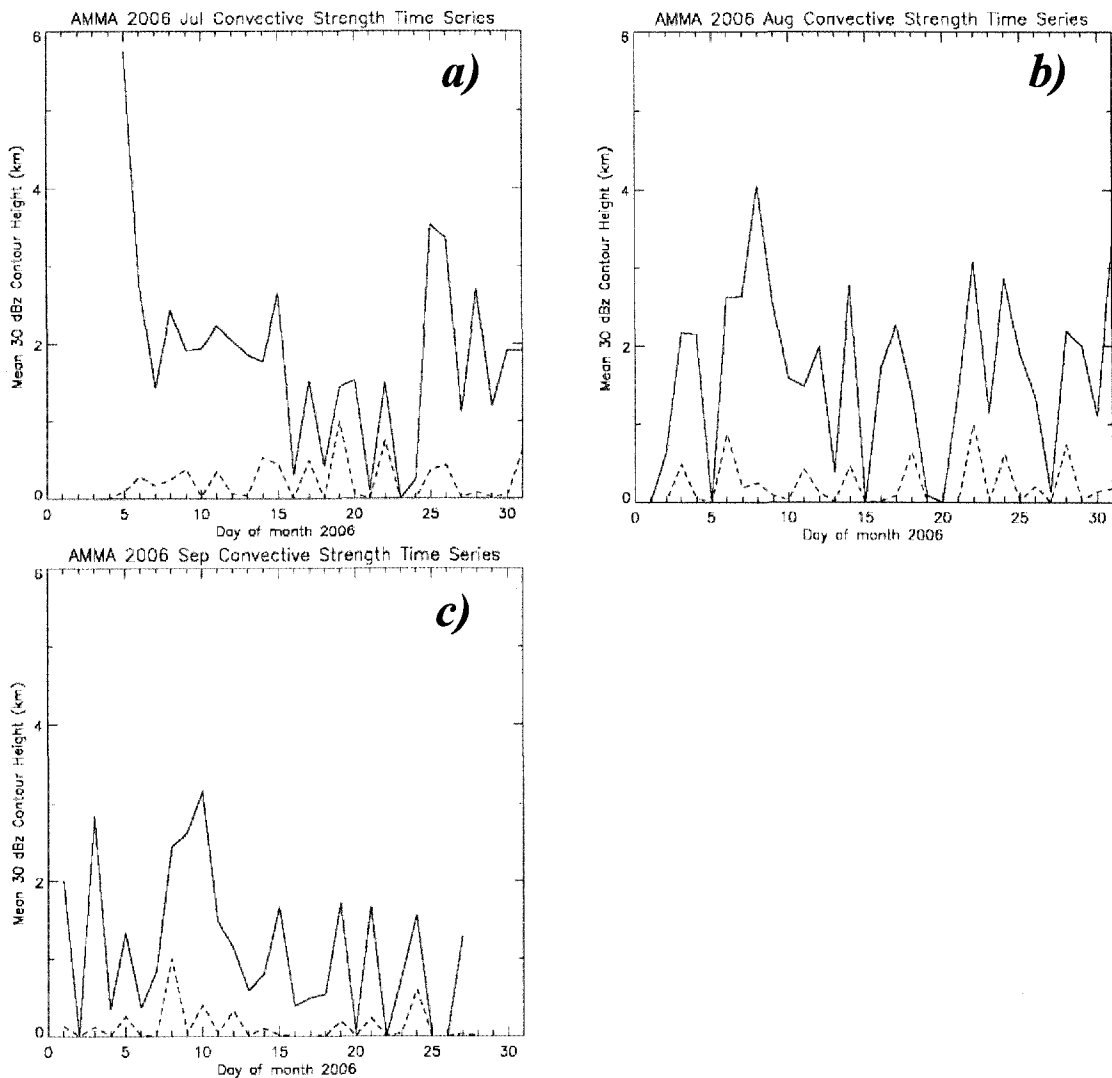


Fig. 37 MIT radar mean 30 dBZ contour height time series (solid line) for a) July, b) August, and c) September 2006. The dashed line indicates daily rainfall normalized against the monthly maximum.

Local maxima of the normalized rainfall series are closely related with peaks in the mean 30 dBZ contour heights, showing a substantial correlation between convective intensity and rainfall. Using the mean 30 dBZ contour height as a measure of intensity suggests that the sub-Saharan region produces intense convective precipitation similar to other tropical regions (Petersen and Rutledge 2001). The WAM reflectivity profiles

suggest behavior much like other continental monsoon regions, with large variability in convective structure, but similar to isolated oceanic regions during the wet season.

f. SLMCSs and AEWs

In parallel with the results of this thesis, Ferreira *et al.* 2008 investigated the relationship between SLMCSs and AEWs. Analysis of Global Precipitation Climatology Project (GPCP) satellite-based observations were used to identify precipitation anomalies, while National Center for Environmental Prediction reanalysis data were used to interpret AEW position over tropical Africa (Ferreira *et al.* 2008). The westward propagation of AEWs was tracked by positive vorticity centers and showed that SLMCSs tended to occur ahead of the passage of an AEW trough during this period, located to the northwest of the AEW trough. Fink and Reiner (1999) suggest a preferential SLMCS formation in the area west of AEW troughs, consistent with Ferreira *et al.* 2008. The change in the central latitude of the ITCZ results in AEW propagation along the northern edge of the ITCZ where flow instability that maintains the waves is maximized. The radar results of this thesis will be integrated with the results of Ferreira *et al.* (2008) in a journal article in preparation.

5. Conclusion

The AMMA summer 2006 intensive observational period provided land-based radar data for the sub-Sahel region of Niamey, Niger. The reflectivity data were used for analysis of structure and propagation of MCSs during the onset and development of the WAM season. Study of relative precipitation of convective systems provided insight into the interaction between MCSs and the surrounding environment. Improved understanding of these WAM characteristics and mechanisms offer valuable information of the hydrological and thermodynamic budget; and improved understanding of the variability and predictability of the WAM.

Radar data provides valuable information regarding storm structure and genesis, but may be hidden by sources of error inherent to radar setups. To obtain reliable and robust data for further detailed analyses, a QC algorithm was applied to the dataset to ensure that egregious artifacts were removed. Many methods have been established for the removal of spurious echo and perform well in a research environment. GSFC has developed one such robust package and made it freely available. The GVS 1C51 software package utilizing a modified version of the Rosenfeld *et al.* (1995) algorithm was employed for the radar data set collected in order to study the 2006 WAM season. The algorithm parameters were optimized for this study to produce the best results in removal of non-meteorological echo, while retaining the greatest amount of valid echo possible.

Once satisfactory removal of false echo was attained, the data were interpolated to a Cartesian grid and mapped as convective and stratiform components, using available

software packages and software packages developed in-house. Final data output revealed substantial suppression of non-meteorological echo, though some stratiform precipitation was sacrificed to obtain optimum performance of the QC algorithm. Resultant convective events showed proficient QC results, with embedded 2nd trip echo proving most difficult for removal. The data has since been requested by and transferred to Meteo-France for future studies, and is available online (http://amma_catalogue.mediasfrance.org/EditDataset.do?datsId=129).

Analysis of precipitation and cloud cover allowed for development of a better understanding of sub-MCS and MCS-scale systems during the WAM. Observed rainfall reached a maximum in August and tapered dramatically in September. Through examination of estimated rainrates and vertical reflectivity structure, July exhibited the most intense convection. Analysis of 30 dBZ contour heights confirmed this result and suggested weak vertical motion and warm rain processes, similar to other continental monsoonal regions.

Rainfall in the Niamey region was associated primarily with SLMCSs, with trailing stratiform squall line structure as observed previously. Convective rainfall contributed slightly more of total rainfall (59%) than the stratiform component, though stratiform cloud cover dominated precipitation areal coverage (87%). Spectral analysis was performed on rainfall time series to attain the expected diurnal convection signal and a signal of 2-4 day passage time, consistent with results from parallel research (Ferreira *et al.* 2008) showing AEW propagation through Niamey.

Future study of individual storm thermodynamic structure may result in a more refined characterization of environmental forcing properties inherent to WAM in the Niamey region. Though not the focus of this study, a statistical analysis of storm propagation and vertical intensity might be combined with spatiotemporal AEW characteristics to gain a greater understanding of sub-Saharan SLMCSs before reaching the western African coast where propagation across the Atlantic is a possibility. Also, quantitative rainfall estimates may be produced as a comparison to rain gauge network data and used as basis of SLMCS tracking via satellite.

REFERENCES

- Aspliden, J. P., Y. Tourre, and J. B. Sabine, 1976: Some climatological aspects of West African disturbance lines during GATE. *Mon. Weather Rev.*, **104**, 1029-1035.
- Barnes, S. L., 1980: Report on a meeting to establish a common Doppler radar data exchange format. *Bull. Amer. Meteor. Soc.*, **61**, 1401-1404.
- Berry, G. J., and C. Thorncroft, 2005: Case study of an intense African easterly wave. *Mon. Wea. Rev.*, **133**, 752-766.
- Berry, G., C. Thorncroft, and T. Hewson, 2007: African easterly waves during 2004 – Analysis using objective techniques. *Mon. Wea. Rev.*, **135**, 1251-1267.
- Blanchard, D. O., 1990: Mesoscale convective patterns of the southern high plains. *Bull. Amer. Meteor. Soc.*, **71**, 994-1005.
- Bluestein, H. B., and M. H. Jain, 1985: Formation of mesoscale lines of precipitation: Severe lines in Oklahoma during the spring. *J. Atmos. Sci.*, **42**, 1711-1732.
- Burpee, R. W., 1972: The origin and structure of easterly waves in the lower troposphere of North Africa. *J. Atmos. Sci.*, **29**, 77-90.
- Cook, K. H., 1999: Generation of the African easterly jet and its role in determining West African precipitation. *J. Climate*, **12**, 1165-1184.
- Cotton, W. R., and R. A. Anthes, 1989: *Storm and Cloud Dynamics*. Academic Press, 883 pp.
- Cressman, G. P., 1959: An operational objective analysis system. *Mon. Wea. Rev.*, **87**, 367-374.
- Daley, R., 1991: Atmospheric Data Analysis. *Cambridge Atmospheric and Space Science Series*, Cambridge University Press. ISBN 0-521-38215-7, 457 pp.
- Demott, C. A., and S. A. Rutledge, 1998: The vertical structure of TOGA COARE convection. Part I: Radar echo distributions. *J. Atmos. Sci.*, **55**, 2730-2747.
- Demott, C. A., and S. A. Rutledge, 1998: The vertical structure of TOGA COARE convection. Part II: Modulating influences and implications for diabatic heating. *J. Atmos. Sci.*, **55**, 2748-2762.

- Dhonneur, G., D. O. Adefolalu, T. Nitta, G. O. P. Obasi, and S. Mbele-Mbong, 1978: The West African Monsoon Experiment (WAMEX). GARP Publication Series (WMO/ICSU), No. 21. GARP, WMO-ICSU Joint Organizing Committee, 88 pp.
- Dolan, B. A., and S. A. Rutledge, 2007: An integrated display and analysis methodology for multivariable radar data. *J. App. Meteor. Climate*, **46**, 1196–1213.
- Doviak, R. J., and D. S. Zrnić, 1993: *Doppler Radar and Weather Observations*. Academic Press, 562 pp.
- Ferreira, R. N., T. M. Rickenbach, N. Guy, and E. R. Williams, 2008: MIT radar observations of the evolution of the West African Monsoon during the AMMA IOP. *28th Conference on Hurricanes and Tropical Meteorology*, Amer. Meteor. Soc., Orlando, FL.
- Fink, A. H., and A. Reiner, 2003: Spatio-temporal variability of the relation between African easterly waves and West African squall lines in 1998 and 1999. *J. Geophys. Res.*, **108**, 4332, doi:10.1029/2002JD002816.
- Fulton, R. A., J. P. Breidenback, D. J. Sea, D. A. Miller, and T. O'Bannon, 1998: The WSR-88D rainfall algorithm. *Wea. Forecasting*, **13**, 377-395.
- Gamache, J. F., and R. A. Houze, Jr., 1982: Mesoscale air motions associated with a tropical squall line. *Mon. Wea. Rev.*, **110**, 118-135.
- Gebremichael, M., T. M. Over, and W. F. Krajewski, 2006: Comparison of the scaling characteristics of rainfall derived from space-based and ground-based radar observations. *J. Hydrometeor.*, **7**, 1277–1294.
- Grist J. P., and S. E. Nicholson, 2001: A study of the dynamic factors influencing the rainfall variability in the West African Sahel. *J. Climate*, **14**, 1337–1359.
- Hall, M. P. M., J. W. F. Goddard, and S. M. Cherry, 1984: Identification of hydrometeors and other targets by dual-polarization radar. *Radio Sci.*, **19**, 132–140.
- Hall, N. M. J., and P. Peyrille, 2006: Dynamics of the West African monsoon. *J. Phys., IV France*, **139**, 85–103.
- Halverson, J. B., T. Rickenbach, B. Roy, H. Pierce, and E. Williams, 2002: Environmental Characteristics of convective systems during TRMM-LBA. *Mon. Wea. Rev.*, **130**, 1493-1509.

- Hartmann, D. L., H. H. Hendon, and R. A. Houze, 1984: Some implications of the mesoscale circulations in tropical cloud clusters for large-scale dynamics and climate. *J. Atmos. Sci.*, **41**, 113–121.
- Hastenrath, S., 1991: *Climate Dynamics of the Tropics*. Kluwer Academic Publishers, 488 pp.
- Houze, R. A., 1977: Structure and dynamics of a tropical squall-line system. *Mon. Wea. Rev.*, **105**, 1540–1567.
- Houze, Jr., R. A., 1993: *Cloud Dynamics*. Academic Press, 573 pp.
- Houze, Jr., R. A., 2004: Mesoscale convective systems, *Rev. Geophys.*, **42**, RG4003, doi:10.1029/2004RG000150.
- Joss, J., and H. Wessels, 1990: Ground clutter suppression for weather radar data. COST Tech. Rep. 73/WD/130, 6 pp.
- Keeler, R. J., and R. E. Passarelli, 1990: Signal processing for atmospheric radars. *Radar in Meteorology*, D. Atlas, Ed., Amer. Meteor. Soc., 199-230.
- Kessinger, C., S. Ellis, and J. VanAndel, 2001: NEXRAD data quality: The AP clutter mitigation scheme. Preprints, *30th Int. Conf. on Radar Meteorology*, Munich, Germany, Amer. Meteor. Soc., 707–709.
- Kiladis, G. N., C. D. Thorncroft, and N. M. J. Hall, 2006: Threedimensional structure and dynamics of African easterly waves. Part I: Observations. *J. Atmos. Sci.*, **63**, 2212–2230.
- Kuettner, J. P., 1974: General description and central program of GATE. *Bull. Amer. Met. Soc.*, **55**, 712-719.
- Kulie, M. S., M. Robinson, D. A. Marks, B. S. Ferrier, D. Rosenfeld, and D. B. Wolff, 1999: Operational processing of ground validation data for the Tropical Rainfall Measuring Mission. Preprints, *29th Int. Conf. on Radar Meteorology*, Montreal, QC, Canada, Amer. Meteor. Soc., 736–739.
- Lakshmanan, V., A. Fritz, T. Smith, K. Hondl, and G. Stumpf, 2007: An automated technique to quality control radar reflectivity data. *J. Appl. Meteor. Climatol.*, **46**, 288-305.
- Laurent, H., N. D’Amato, and T. Lebel, 1998: How important is the contribution of the mesoscale convective complexes to the Sahelian rainfall? *Phys. Chem. Earth*, **23**, 629-633.

- Le Barbé, L., and T. Lebel, 1997: Rainfall climatology of the HAPEX-Sahel region during the years 1950-1990. *J. Hydrol.*, **188**, 74-96.
- Lebel, T., H. Sauvageot, M. Hoepffner, M. Desbois, B. Guillot, and P. Hubert, 1992: Rainfall estimation in the Sahel: The EPSAT-Niger experiment. *Hydrol. Sci. J.*, **37**, 201-215.
- Lee, R., G. Della Bruna, and J. Joss, 1995: Intensity of ground clutter and of echoes of anomalous propagation and its elimination. Preprints, *27th Conf. on Radar Meteorology*, Vail, CO, Amer. Meteor. Soc., 651-652.
- LeMone, M. A., G. M. Barnes, and E. J. Zipser, 1984: Momentum flux by lines of cumulonimbus over the tropical ocean. *J. Atmos. Sci.*, **41**, 1914-1932.
- Leroux, M., 2001: *The Meteorology and Climate of Tropical Africa*. Praxis Publishing Ltd., 548 pp.
- Machado, L. A. T., J.-P. Duvel, and M. Desbois, 1993: Diurnal variations and modulation by easterly waves of the size distribution of convective cloud clusters over West Africa and the Atlantic Ocean. *Mon. Wea. Rev.*, **121**, 37-49.
- Maddox, R. A., 1980: Mesoscale convective complexes. *Bull. Amer. Met. Soc.*, **61**, 1374-1387.
- Mapes, B. E., and R. A. Houze Jr., 1995: Diabatic divergence profiles in western Pacific mesoscale convective systems, *J. Atmos. Sci.*, **52**, 1807-1828.
- Marks, D. A., M. S. Kulie, M. Robinson, D. S. Silberstein, D. B. Wolff, B. S. Ferrier, E. Amitai, B. Fisher, J. Wang, D. Augustine, and O. Thiele, 2000: Climatological processing and product development for the TRMM Ground Validation program. Physics and chemistry of the Earth, (PCE), Part B. *Hydrol., Oceans Atmos.*, **25**, 871-876.
- Mathon, V., and H. Laurent, 2001: Life cycle of the Sahelian mesoscale convective cloud systems. *Quart. J. Roy. Meteor. Soc.*, **127**, 377-406.
- Mathon, V., H. Laurent, and T. Lebel, 2002: Mesoscale convective system rainfall in the Sahel. *J. Appl. Meteor.*, **41**, 1081-1092.
- Matthews, A. J., 2004: Intraseasonal variability over tropical Africa during northern summer. *J. Climate*, **17**, 2427-2440.

- Mekonnen, A., C. D. Thorncroft, and A. R. Aiyyer, 2006: Analysis of convection and its association with African easterly waves. *J. Climate*, **19**, 5405-5421.
- Mohr, C. G., and R. L. Vaughan, 1979: An economical procedure for Cartesian interpolation and display of reflectivity factor data in three-dimensional space. *J. Appl. Meteor.*, **18**, 661-670.
- Mohr, C. G., L. J. Miller, R. L. Vaughn, and H. W. Frank, 1986: The merger of mesoscale datasets into a common Cartesian format for efficient and systematic analyses. *J. Atmos. Oceanic Technol.*, **3**, 143-161.
- Moncrieff, M. W., 1981: A theory of organized steady convection and its transport properties. *Quart. J. Roy. Meteor. Soc.*, **107**, 29-50.
- Mueller, E. A., and A. L. Sims, 1975: Statistics of high radar reflectivity gradients. Preprints, *16th Radar Meteorology Conf.*, Houston, TX, Amer. Meteor. Soc., 401-403.
- Payne, S. W., and M. M. McGarry, 1977: The relationship of satellite inferred convective activity to easterly waves over West Africa and the adjacent ocean during phase III of GATE. *Mon. Wea. Rev.*, **105**, 413-420.
- Petersen, W. A., and S. A. Rutledge, 2001: Regional variability in tropical convection: Observations from TRMM. *J. Climate*, **14**, 3566-3586.
- Pratte, F., D. Ecoff, and J. VanAndel, 1996: AP ground clutter in WSR-88D base data and recommendations for automatic AP clutter mitigation. FY96 Report. NWS/OSF Engineering Branch, 29 pp.
- Pratte, J. F., R. Gagnon, and R. Cornelius, 1993: Ground clutter characteristics and residue mapping. Preprints, *26th Int. Conf. on Radar Meteorology*, Norman, OK, Amer. Meteor. Soc., 50-52.
- Pratte, J. F., R. J. Keeler, R. Gagnon, and D. Sirmans, 1995: Clutter processing during anomalous propagation conditions. Preprints, *27th Conf. on Radar Meteorology*, Vail, CO. Amer. Meteor. Soc., 139-141.
- Redelsperger, J. L., C. D. Thorncroft, A. Diedhiou, T. Lebel, D. J. Parker, and J. Polcher, 2006: African Monsoon Multidisciplinary Analysis: An International Research Project and Field Campaign. *Bull. Amer. Met. Soc.*, **87**, 1739-1746.
- Reed, R. J., D. C. Norquist, and E. E. Recker, 1977: The structure and properties of African wave disturbances as observed during Phase III of GATE. *Mon. Wea. Rev.*, **105**, 317-333.

- Rickenbach, T. M., 2004: Nocturnal cloud systems and the diurnal variation of clouds and rainfall in southwestern Amazonia. *Mon. Wea. Rev.*, **132**, 1201-1219.
- Rickenbach, T. M., and S. A. Rutledge, 1998: Convection in TOGA COARE: Horizontal scale, morphology, and rainfall production. *J. Atmos. Sci.*, **55**, 2715-2729.
- Rickenbach, T. M., R. N. Ferreira, J. B. Halverson, D. L. Herdies, and M. A. F. Silva Dias, 2002: Modulation of convection in the southwestern Amazon basin by extratropical stationary fronts. *J. Geophys. Res.*, 107(D20), 8040, doi:10.1029/2000JD000263.
- Rinehart, R. E., 1997: *Radar for Meteorologists*. Rinehart Publications, 428 pp.
- Robinson, M., M. Steiner, D. B. Wolff, C. Kessinger, and R. A. Fulton, 2001: Radar data quality control: Evaluation of several algorithms based on accumulating rainfall statistics. Preprints, 30th Int. Conf. on Radar Meteorology, Munich, Germany, Amer. Meteor. Soc., 274-276.
- Rosenfeld, D., E. Amitai, and D. B. Wolff, 1995: Classification of rain regimes by the three-dimensional properties of reflectivity fields. *J. Appl. Meteor.*, **34**, 198-211.
- Rowell, D. P., and J. R. Milford, 1993: On the generation of African squall lines. *J. Climate*, **6**, 1181-1193.
- Ryzhkov, A., D. Zrnica, and D. Atlas, 1996: Polarimetrically tuned R(Z) relations and comparison of radar rainfall methods. *J. Appl. Meteor.*, **36**, 340-349.
- Sauvageot, H., and J. P. Lacaux, 1995: The shape of averaged drop size distributions. *J. Atmos. Sci.*, **52**, 1070-1083.
- Schmidt, J. M., and W. R. Cotton, 1990: Interactions between upper and lower tropospheric gravity waves on squall line structure and maintenance, *J. Atmos. Sci.*, **47**, 1205-1222.
- Schumacher C., and R. A. Houze, Jr., 2006: Stratiform precipitation production over sub-Saharan Africa and the tropical East Atlantic as observed by TRMM. *Q. J. R. Meteorol. Soc.*, **132**, 2235-2255.
- Shinoda, M., T. Okatani, and M. Saloum, 1999: Diurnal variations of rainfall over Niger in the west African Sahel: A comparison between wet and drought years. *Int. J. Climatol.*, **19**, 81-94.

- Sultan, B., and S. Janicot, 2003: The West African monsoon dynamics. Part I: Documentation of intraseasonal variability. *J. Climate*, **16**, 3389-3406.
- Sultan, B., and S. Janicot, 2003: The West African monsoon dynamics. Part II: The “preonset” and “onset” of the summer monsoon. *J. Climate*, **16**, 3407-3427.
- Smith, P. L., 1990: Precipitation measurement and hydrology: Panel report. *Radar in Meteorology*, D. Atlas, Ed., Amer. Meteor. Soc., 607-618.
- Steiner, M., and J. Smith, 2002: Use of three-dimensional reflectivity structure for automated detection and removal of nonprecipitating echoes in radar data. *J. Atmos. Oceanic Technol.*, **19**, 673-686.
- Steiner, M., R. A. Houze, and S. E. Yuter, 1995: Climatological characteristics of three-dimensional storm structure from operational radar and raingauge data. *J. Appl. Meteor.*, **34**, 1978-2007.
- Thorncroft, C., and K. Hodges, 2001: African easterly wave variability and its relationship to Atlantic tropical cyclone activity. *J. Climate*, **14**, 1166-1179.
- Yuter, S. E. and R. A. Houze, Jr., 1995: Three-dimensional kinematic and microphysical evolution of Florida cumulonimbus. Part II: Frequency distributions of vertical velocity, reflectivity, and differential reflectivity. *Mon. Wea. Rev.*, **123**, 1941-1963.
- Zipser, E. J., 1977: Mesoscale and convective-scale downdrafts as distinct components of squall-line circulation. *Mon. Wea. Rev.*, **105**, 1568-1589.
- Zipser, E. J., and K. R. Lutz, 1994: The Vertical Profile of Radar Reflectivity of Convective Cells: A Strong Indicator of Storm Intensity and Lightning Probability? *Mon. Wea. Rev.*, **122**, 1751-1759.

APPENDICES

Appendix A List of Symbols

R	rainfall rate
Z	radar reflectivity
Z_{dBZ}	radar reflectivity threshold
Z_{max}	maximum reflectivity value
Z_{top}	echo top height
h	height

Appendix B List of Acronyms

AEJ	African Easterly Jet
AEW	African Easterly wave
AGL	Above ground level
AP	Anomalous propagation
AMMA	African Monsoon Multidisciplinary Activities
CAPE	Convective Available Potential Energy
CAPPI	Constant Altitude Plan Position Indicator
CDF	network Common Data Form
CIN	Convective Inhibition
DSD	Drop size distribution
EPSAT	Etudes des Precipitations par Satellite
FFT	Fast Fourier transform
GARP	Global Atmospheric Research Project
GATE	GARP Atlantic Tropical Experiment
GSFC	Goddard Space Flight Center
GVS	Ground Validation System
IR	Infrared
IRIS	Interactive Radar Information System
IDL	Interactive Data Language
ITCZ	Intertropical convergence zone
ITF	Inter-tropical front

LT	Local time
LW	Long-wave radiation
MCC	Mesoscale convective complex
MCS	Mesoscale convective system
MIT	Massachusetts Institute of Technology
OCS	Organized convective system
PRF	Pulse repetition frequency
QC	Quality control
RHI	Range Height Indicator
RSL	Radar Software Library
SAL	Saharan air layer
SJSU	San Jose State University
SLMCS	Squall line MCS
SW	Short-wave radiation
TRMM	Tropical Rainfall Measurement Mission
TSVO	TRMM Satellite Validation Office
UF	Universal format
UTC	Universal Coordinated Time
WAM	West African Monsoon
WAMEX	West African Monsoon Experiment
Z-R	Reflectivity - rainfall rate